catalysts

Article

Mechanistic Details of the Sharpless Epoxidation of Allylic Alcohols—A Combined URVA and Local Mode Study

Marek Freindorf † **and Elfi Kraka** *,†

Chemistry Department, Southern Methodist University, 3215 Daniel Avenue, Dallas, TX 75275-0314, USA; mfreindorf@smu.edu
* Correspondence: ekraka@smu.edu
† These authors contributed equally to this work.

Abstract: In this work, we investigated the catalytic effects of a Sharpless dimeric titanium (IV)–tartrate–diester catalyst on the epoxidation of allylalcohol with methyl–hydroperoxide considering four different orientations of the reacting species coordinated at the titanium atom (reactions **R1**–**R4**) as well as a model for the non–catalyzed reaction (reaction **R0**). As major analysis tools, we applied the URVA (Unified Reaction Valley Approach) and LMA (Local Mode Analysis), both being based on vibrational spectroscopy and complemented by a QTAIM analysis of the electron density calculated at the DFT level of theory. The energetics of each reaction were recalculated at the DLPNO-CCSD(T) level of theory. The URVA curvature profiles identified the important chemical events of all five reactions as peroxide OO bond cleavage taking place before the TS (i.e., accounting for the energy barrier) and epoxide CO bond formation together with rehybridization of the carbon atoms of the targeted CC double bond after the TS. The energy decomposition into reaction phase contribution phases showed that the major effect of the catalyst is the weakening of the OO bond to be broken and replacement of OH bond breakage in the non–catalyzed reaction by an energetically more favorable TiO bond breakage. LMA performed at all stationary points rounded up the investigation (i) quantifying OO bond weakening of the oxidizing peroxide upon coordination at the metal atom, (ii) showing that a more synchronous formation of the new CO epoxide bonds correlates with smaller bond strength differences between these bonds, and (iii) elucidating the different roles of the three TiO bonds formed between catalyst and reactants and their interplay as orchestrated by the Sharpless catalyst. We hope that this article will inspire the computational community to use URVA complemented with LMA in the future as an efficient mechanistic tool for the optimization and fine-tuning of current Sharpless catalysts and for the design new of catalysts for epoxidation reactions.

Keywords: Sharpless epoxidation; Unified Reaction Valley Approach (URVA); local vibrational mode theory; reaction mechanism; bond strength analysis; methy–hydroperoxide epoxidation of allylalcohol

check for updates

Citation: Freindorf, M.; Kraka, E. Mechanistic Details of the Sharpless Epoxidation of Allylic Alcohols—A Combined URVA and Local Mode Study. *Catalysts* **2022**, *12*, 789. https://doi.org/10.3390/catal12070789

Academic Editor: Antonio Monopoli

Received: 17 June 2022
Accepted: 14 July 2022
Published: 18 July 2022

1. Introduction

Epoxides (also known as oxiranes) are classes of compounds with two carbon atoms connected to an oxygen atom forming a three-membered ring (3MR). Due to the ring strain and polarization of the C-O bonds in the 3MR, the epoxide group is highly reactive, making epoxides valuable chemical intermediates stretching from organic synthesis and catalysis [1–5], the design of polymers and materials, e.g., based on natural terpene epoxides [6] to their use as raw materials in various industries producing fine chemicals for pharmaceuticals, fragrances, food or other agricultural products [7–16]. Ethylene oxide and propylene oxide are among the highest volume products in our industry, with annual production rates of 15 and 3 Mt per year, respectively [1]. The major source of epoxide intermediates is the epoxidation of olefins [17–22]. In nature, there exist various enzymes that are capable of oxidizing target substrates with high selectivity to produce epoxides [23–26].

Optically enriched epoxides are important heterocyclic intermediates for enantioselective synthesis [27–29], including natural and bioactive products [2,30], or agrochemicals, such as fungicides, herbicides, insecticides and pheromones [8]. A pure enantiomeric product is even more important in pharmaceutical industry, where high enantiomeric excess is needed due to the different physiological effects that one enantiomer can show after interacting with a chiral biological target [14,16,31–34].

There are different routes for the synthesis of epoxides, such as oxidation of alkenes [35] or the reaction of alkenes with peroxides [36,37] or often supported by catalysts [1,7]. The epoxidation of allyl alcohols with peroxides leads to important raw materials for the production of glycerol and is also used as a precursor to many specialized compounds, such as flame-resistant materials, drying oils and plasticizers [38].

In 1980s, a breakthrough in the asymmetric epoxidation of primary and secondary allylic alcohols was achieved by Katsuki and Sharpless, who reported the enantioselective synthesis of 2,3-epoxyalcohols in the presence of hydroperoxide, (mostly t-butylhydroperoxide, TBHP), a titanium (IV) isopropoxide (O^{i}Pr)$_4$) catalyst and a chiral diethyl tartrate (DET) [39,40].

This pioneering work, for which Sharpless was awarded with the 2001 Nobel Prize in Chemistry [41] has inspired the field since then [14,29,30,42–53], leading to a variety of modified and new catalysts for the asymmetric epoxidation [12–14,27,33,54–60], including the Jacobsen-Katsuki epoxidation [61], the Prilezhaev reaction [7,10], or the Shi expoxidation [62], to mention a few, and in 2021 to another Noble Prize in Chemistry being awarded to Benjamin List and David MacMillan for their development work in asymmetric organocatalysis [63].

As sketched in Figure 1a the stereochemistry of the product is promoted via the chiral dimeric Ti complex formed via rapid ligand exchange of (O^{i}Pr) and DET controlling the chirality of the epoxidation reaction [39,40,64]. As depicted in Figure 1b, the catalyst mimics a heterogenous surface with the oxidant peroxide binding to the Ti center on one side and the allylic alcohol on the opposite site. Via an η^2–coordinate transition state (TS) the peroxide oxygen bound to Ti is transferred to the CC double bond of the allylic alcohol to be attacked and the resulting epoxide is formed with more than 90% enantiomeric excess [39,40].

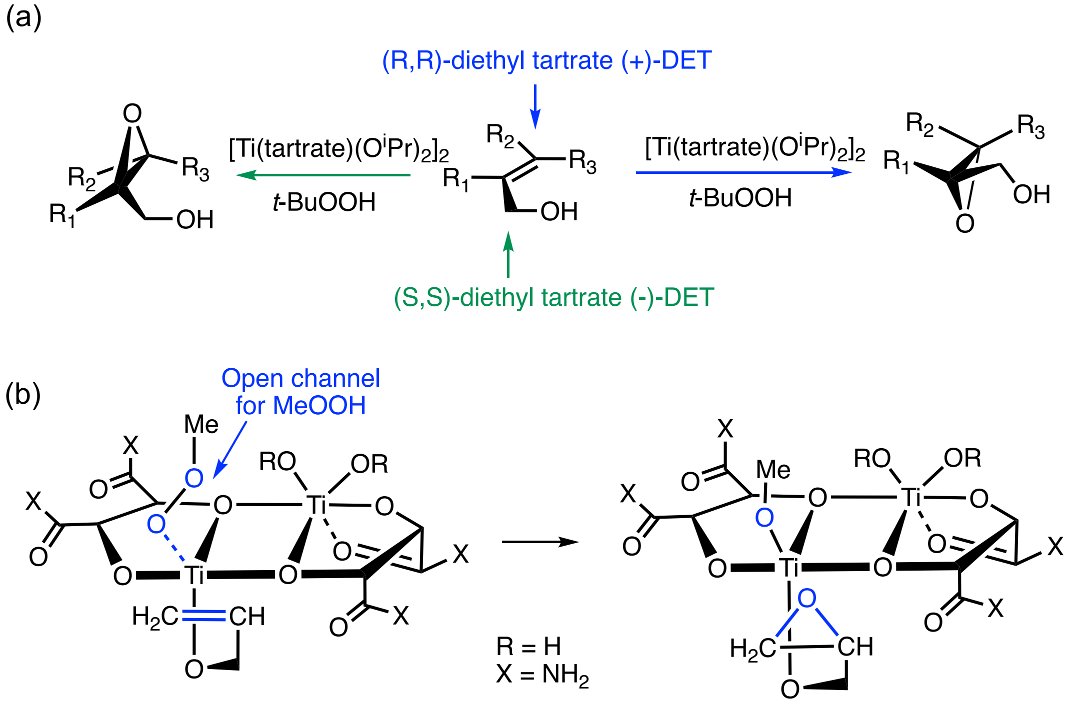

Figure 1. Sharpless asymmetric epoxidation (**a**) General scheme; (**b**) Dimeric Sharpless titanium(IV) model catalyst for the methyl–hydroperoxide oxidation of allylalcohol studied in this work.

Compared to the large number of experimental studies published, theoretical work elucidating mechanistic details of the Ti–tartrate catalyst at the atomistic level is still sparse [64–70]. According to the previous theoretical studies based on the orbital analysis, a spiro orientation of TS is preferred over a planar orientation. Two important interactions in the reaction complex (RC) were identified, i) the interaction between a lone pair of the peroxide oxygen atom with a π^* orbital of the alkene and ii) the interaction of a TiO antibonding orbital with a π orbital of the alkene [65]. Wu and Lai dismissed the monomeric mechanism proposed by Corey [66,71].

The dependence of the catalytic activity on the bulky peroxide and the tartrate ligands was discussed as well as solvent effects on diastereoselectivity [69]. Although these are valuable insights, still missing is a comprehensive understanding on how the catalyst efficiently supports the attack of the peroxide to the CC double bond; a prerequisite for fine-tuning of existing and the design of new Sharpless-type catalysts.

Therefore, in this work, we investigated the main reaction step of the epoxidation cycle, which involves OO bond cleavage of the peroxide group, the transfer of the O atom from the peroxide to the CC double bond of the allylic group and the formation of two CO bonds leading to the epoxide of the final product [54] for the epoxidation of methyl–hydroperoxide and allyl alcohol using the dimeric Ti model catalyst shown in Figure 1b. Four different orientations of the reacting species were considered labeled as **R1**, **R2**, **R3** and **R4** in Figure 2. The initial catalyst geometry was taken from the x–ray structure of the complex of reaction **R4** [44].

In order to better understand the catalytic effect of the titanium(IV) dimer catalyst, we also investigated the non–catalytic epoxidation reaction. The non–catalyzed reaction between methyl–hydroperoxide and allylic alcohol leads to the formation of hydrogen bonds between these molecules and as such to a quite different mechanism than that of the catalyzed reaction, particularly in the entrance channel, which makes a direct comparison with the catalyzed reactions difficult. Therefore, as a simplified model of the non–catalyzed reaction, we chose the reaction between methyl–hydroperoxide and propene, which is labeled as reaction **R0** in Figure 2.

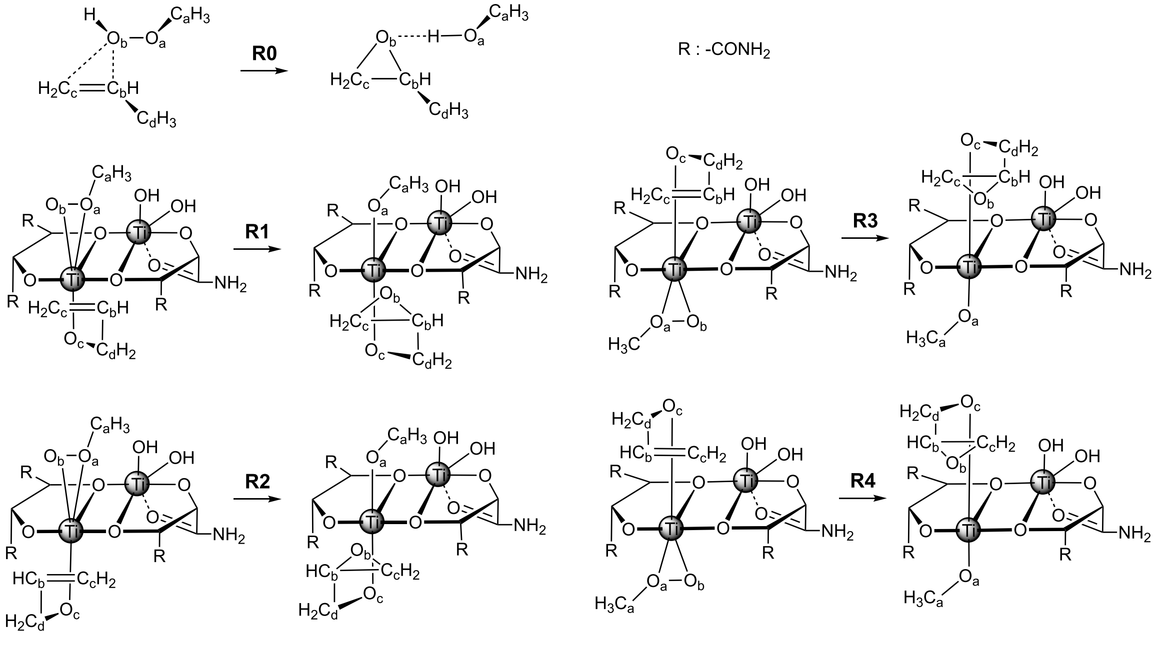

Figure 2. Schemes of the chemical reactions investigated in this study. **R0**: non–catalyzed reaction, **R1**–**R4**: catalyzed reactions with different orientation of the reactants coordinated at one of the Ti atoms.

The major focus of our study was to explore how the catalyst changes OO bond breaking and CO bond forming compared to the non–catalyzed epoxidation reaction. As major tools we applied the *Unified Reaction Valley Approach* (URVA) [72] and the *Local Mode Analysis* (LMA) [73], both based on vibrational spectroscopy, complemented with Bader's *Quantum Theory of Atoms in Molecules* (QTAIM) [74–77] and the *Natural Bond Orbital* (NBO) analysis [78–80]. The manuscript is structured in the following way; first computational details are presented followed by the results and discussion part. Conclusion are summarized in the final part of the manuscript.

2. Computational Methods

We utilized URVA to monitor and analyze the OO bond breakage and the formation of the new CO bonds during the epoxidation reaction. A comprehensive review of URVA is presented in Ref. [72] and the theoretical background of URVA is further described in Refs. [81–83]; therefore, in the following, only some essential features are summarized. URVA analyses a chemical reaction along a representative reaction path, which is traced out by the reaction complex (RC), i.e., the union of reacting molecules on the potential energy surface (PES) during its way from the entrance channel via the transition state (TS) to the exit channel of the reaction.

As the reaction proceeds, the electronic structure of the RC changes, which is registered by vibrational modes perpendicular to the long amplitude motion along the reaction path spanning the so-called *Reaction Valley*. As described in the seminal Miller, Handy and Adams paper on the *Reaction Path Hamiltonian*, these transverse vibrational modes couple with the translational motion along the reaction path and the sum of all coupling elements defines the scalar reaction path curvature [84].

Hence, any chemical changes involving electronic structure reorganizations, such as bond formations, bond cleavages or conformational changes, are reflected by changes in the scalar reaction path curvature, leading to a specific curvature pattern with curvature maxima (defining the locations of chemical change along the reaction path) flanked by curvature minima (defining locations of minimal electronic structure changes, often reflecting the beginning of a new chemical event and/or the locations of hidden intermediates [85]) dividing the entire reaction path into chemically meaningful reaction phases. In this way, the reaction path curvature profile can be considered as the so-called *finger print* of the reaction [85,86].

The scalar curvature is decomposed into geometrical components representing bond lengths, bond angles, dihedral angles, puckering coordinates, pyramidalization angles, etc. [81] providing detailed information about which part of the RC is involved in a certain chemical event. A positive sign of a contribution of a particular component to the reaction curvature corresponds to a supporting effect of this component to the electronic structure reorganization from the reactant to product along the reaction path, and a negative sign indicates a resisting effect.

Only chemical events occurring before the TS contribute to the energy barrier, and thus the careful analysis of the curvature peaks in the entrance provides useful information on how to lower the barrier [72]. Some selected applications including enzyme studies demonstrating how URVA unravels even small mechanistic details can be found in Refs. [82,85–94].

We used LMA, which is also based on vibrational spectroscopy, in order to complement the URVA results via a comprehensive bond strength analysis of the peroxide OO bond, the emerging CO bonds, the CC double bond of the alcohol as well as the three TiO bonds (catalyzed reactions) and alternatively the OH bonds and hydrogen shift (non–catalyzed reaction) at the stationary points on the PES (i.e., reactant complex, TS and product complex) for each of the five reactions investigated. The theoretical background of LMA, originally developed by Konkoli and Cremer [95–99] can be found in a comprehensive review article [73].

The local vibrational modes of a molecule can be considered as the local counterparts of normal vibrational modes, which are generally delocalized due to electronic and mass–coupling [100,101], disqualifying related normal mode stretching force constants as individual bond strength descriptors. In contrast, local vibrational stretching force constants derived from uncoupled local vibrational modes directly reflect the intrinsic strength of a chemical bond and/or weak chemical interaction [73,102].

LMA has been effectively used to characterize covalent bonds [86,102–113], hydrogen bonding [114–122], halogen bonding [123–129], pnicogen bonding [129–132], chalcogen bonding [111,129,133], tetrel bonding [134] and to characterize specific properties, such as a BH$\cdots\pi$ interaction [135,136], an aromaticity index [137–139], a metal electronic parameter [120,125,138,140–144] and a vibrational Stark effect [145]. LMA has also been successfully applied in combined QM/MM calculations [91,146–148], and periodic DFT calculations [149,150].

Local mode force constants k^a can be transformed into bond strength orders (BSO), which are more chemically intuitive bond strength descriptors by using a power relationship according to the generalized Badger rule with $BSO = A * (k^a)^B$ [86,151]. The parameters A and B are obtained from two reference molecules for each bond type under investigation, with known BSO and k^a values and the requirement that the BSO for a zero force constant k^a is also zero.

In our study, we used the following reference molecules and data summarized in Table 1: for OO bonds H_2O_2 (BSO = 1, k^a = 4.169 mDyn/Å) and O_2 (BSO = 2, k^a = 12.968 mDyn/Å); for CC bonds, C_2H_6 (BSO = 1, k^a = 4.141 mDyn/Å) and C_2H_4 (BSO = 2, k^a = 9.910 mDyn/Å); for CO bonds, CH_3OH (BSO = 1, k^a = 4.905 mDyn/Å) and CH_2O (BSO = 2, chose TiOH (BSO = 1.1543, k^a = 3.301 mDyn/Å) and TiO (BSO = 2.3034, k^a = 7.979 mDyn/Å) as reference molecules, where Mayer bond orders were used instead of single and double bonds [152–154]. Those values were used to calculate the A and B parameters for each bond type, which are presented in the corresponding plots URVA plots. The local mode force constants k^a of the reference molecules were calculated at the B3LYP/6-31G(d,p)/SDD(Ti) level of theory.

Table 1. The molecule, bond length d, local mode force constant k^a, bond strength order BSO and energy density at the bond critical point H_ρ, for the reference molecules. B3LYP/6-31G(d,p)/SDD(Ti) level of theory.

	Single Bond					**Double Bond**				
Bond	**Molecule**	**d**	**k^a**	**BSO**	**H_ρ**	**Molecule**	**d**	**k^a**	**BSO**	**H_ρ**
		Å	**mDyn/Å**		**Hr/Bohr^3**		**Å**	**mDyn/Å**		**Hr/Bohr^3**
CC	C_2H_6	1.530	4.141	1	−0.1932	C_2H_4	1.330	9.910	2	−0.3932
CO	CH_3OH	1.418	4.905	1	−0.3719	CH_2O	1.207	13.607	2	−0.6883
OO	H_2O_2	1.456	4.169	1	−0.2203	O_2	1.214	12.968	2	−0.6305
TiO	TiOH	1.804	3.301	1	−0.0265	TiO	1.612	7.979	2	−0.1628
OH	H_2O	0.965	8.216	1	−0.5882	F_2H^{-1}	1.150	1.203	0.5	−0.1951

LMA was complemented with QTAIM, which provides additional bonding details via the topological features of the total electron density $\rho(\mathbf{r})$ [74–77]. QTAIM allows assessing the covalent character of bonds using the Cremer–Kraka criterion of covalent bonding [155–157]. The criterion is based on two conditions, a necessary and a sufficient one. The necessary condition requires the existence of a bond path and a bond critical bond critical point ρ of the electron density between the two atoms under consideration. The sufficient condition requires that the energy density H_ρ at the bond critical point is negative.

H_ρ is defined as: $H_\rho = G_\rho + V_\rho$, where G_ρ is the kinetic energy density and V_ρ is the potential energy density. A negative V_ρ corresponds to an accumulation of the electron density, whereas a positive G_ρ corresponds to a depletion of the electron density [156]. As a result, the sign of H_ρ indicates which term is dominant [157]. Therefore, for $H_\rho < 0$, the interaction is considered as covalent in nature, whereas for $H_\rho > 0$, the interaction has predominantly electrostatic character.

We used the intrinsic reaction coordinate (IRC) path of Fukui [158] as the reaction path. All IRC calculations were performed with the improved reaction path following the procedure of Hratchian–Kraka [159], which allows us to accurately trace the reaction path and its curvature far into the entrance and exit channel and leads to reliable vibrational frequencies along the IRC, which are needed to span the reaction valley. The stationary point calculation and the IRC procedure were performed with DFT using the B3LYP functional [160–163] combined with the 6-31G(d,p)/SDD(Ti) basis set [164–166].

The energetics of the investigated chemical reactions were recalculated by performing single point energy calculations at the DLPNO-CCSD(T)/def2-TZVP level of theory [167,168], based on DFT geometries and applying thermochemical corrections from the DFT calculations. The DFT calculations were performed with Gaussian [169], and the single point energy calculations with DLPNO-CCSD(T) were done using ORCA [170]. The URVA analysis was conducted with the program pURVA [171]. The LMA analysis was done with the LModeA program [172]. The atomic charges along the reaction path were calculated using the NBO program [78]. The QTAIM analysis was performed with the AIMALL program [173].

3. Results and Discussion

In the following, the energetics, the reaction path properties along the reaction path and a chemical bond analysis are presented for each of the reactions **R0**–**R4**. Reaction movies **R0**–**R4** illustrating the movement of the atoms for each RC during the epoxidation process can be found in the Supplementary Materials.

3.1. Energetics

Table 2 presents the activation and reaction energies as well the activation and reaction enthalpies of reactions **R0**–**R4** investigated in our study based on DFT calculations using the B3LYP/6-31G(d,p)/SDD(Ti) level of theory. All energies/enthalpies are given relative to the last point on the IRC (van der Waals complex). Table 2 also shows single point DLPNO-CCSD(T)/def2-TZVP energies and enthalpies based on the DFT geometries.

For the DLPNO-CCSD(T) enthalpies, thermochemistry corrections were taken from the corresponding DFT calculations. The following discussion of the energetics is based on the results of the DLPNO-CCSD(T) calculations. According to Table 2, the activation energy of the non–catalyzed reaction **R0** has a value of 38.1 kcal/mol, which is almost 100% larger than the activation energies of the catalyzed reactions with values in the range between 22.3 and 24.4 kcal/mol, thus, showing a substantial effect of the catalyst. The smallest activation energies were obtained for reactions **R3** and **R4** (22.3 and 22.5 kcal/mol, respectively), where the orientation of the reacting species is opposite relative to that in reactions **R1** and **R2** (see Figure 2) with a slightly larger activation energy value of 24.4 kcal/mol.

All five reactions are exothermic, the non–catalyzed reaction **R0** has (with a value of −48.0 kcal/mol) the largest exothermicity compared to the catalyzed reactions with values in a range between −39.9 and −41.9 kcal/mol. According to our results as presented in Table 2, the activation enthalpies of all reactions are generally smaller than the activation energies, while the reaction enthalpies are less negative, showing small thermal effects on the overall energetics of the investigated reactions. The energy barriers show the overall effect of the catalyst; however, they do not provide mechanistic details, which will be discussed in the next section based on URVA.

Table 2. Activation and reaction energy E^a, E_R and activation and reaction enthalpy H^a, H_R (kcal/mol) of reactions **R0**–**R4** investigated in this study. All energies/enthalpies are given relative to the last point on the IRC (van der Waals complex). B3LYP/6-31G(d,p)/SDD(Ti) and DLPNO-CCSD(T)/def2-TZVP levels of theory.

	DFT				**DLPNO-CCSD(T)**			
Reaction	**E^a**	**E_R**	**H^a**	**H_R**	**E^a**	**E_R**	**H^a**	**H_R**
R0	38.6	−46.0	36.4	−44.7	38.1	−48.0	35.8	−46.6
R1	21.2	−43.2	19.9	−42.8	24.4	−41.9	23.2	−41.5
R2	22.6	−40.6	21.2	−39.7	24.4	−40.3	23.1	−39.3
R3	19.6	−40.7	18.3	−40.3	22.3	−39.9	20.9	−39.6
R4	21.1	−40.6	19.8	−40.1	22.5	−40.4	21.2	−40.0

Table 3 shows the relative energies of reactants, TSs and products for reactions **R1**–**R4** with regard to the corresponding stationary points of reaction **R3** based on the DLPNO-CCSD(T)/def2-TZVP levels of theory. Reaction **R3** has the most stable reactant of the four reactions **R1**–**R4**, followed by **R2**, **R4** and **R1** (relative energies of 0.5, 1.1 and 2.1 kcal/mol, respectively), although the energy differences are small. Similarly, the TS of reaction **R3** is energetically lower by 4.2 kcal/mol relative to that of **R1**, by 2.6 kcal/mol relative to that of reaction **R2** and 1.2 kcal/mol relative to that of reaction **R4**, respectively.

Energy differences among the four products are only marginal. In summary, reaction **R3** has the most stable reactant, TS and product compared to the other reactions, which is a cumulative effect of the most effective electrostatic interaction between the positively charged H atom of the reacting species (the methyl group of methyl–hydroperoxide and the propene group of allylalcohol) and the negatively charged oxygen atoms of the catalyst, which are in closer proximity in the orientation of the reacting species of reaction **R3**, an observation that could be further explored in future catalyst tuning efforts.

Table 3. The relative energies (kcal/mol) of reactants, TSs and products for **R1**–**R4** taking reaction **R3** as a reference. DLPNO-CCSD(T)/def2-TZVP levels of theory.

Reaction	**Reactant**	**TS**	**Product**
R1	2.1	4.2	0.1
R2	0.5	2.6	0.1
R3	0.0	0.0	0.0
R4	1.1	1.2	0.6

3.2. Reaction Mechanism

*Reaction **R0***: Selected reaction properties along the reaction path obtained from the URVA analysis of reaction **R0** are presented in Figure 3. The URVA analysis of the non–catalyzed reaction **R0** starts the entrance channel from a van der Waals complex. According to our calculations, the methyl–hydroperoxide approaches the allyl alcohol via the OH oxygen, which is closer to the methyl substituted carbon of the CC double bond (Figure 2). This is followed by the cleavage of the peroxide OO bond, the elongation of the CC double bond and the formation of the O_bC_b and O_bC_c epoxide bonds (see movie R0 of the Supplementary Material and Figure 2).

According to the curvature profile in Figure 3b, the reaction is composed of 11 phases with the first two phases being devoted to the proper alignment of peroxide and alcohol. In phase 4, the OO bond of the peroxide group starts to cleave, which is reflected by a supporting contribution of the O_aO_b distance to the large reaction path curvature peak in this phase (red line in Figure 3b), whereas the formation of the new CO bonds starts already in phase 3 with smaller resisting contributions to this curvature peak (O_bC_b bond blue line and O_bC_c bond green line in in Figure 3b).

The starting process of OO bond breakage is in line with the change of the O_aO_b bond length, which starts to elongate in phase 4, as shown in Figure 3c, and by a change of the O_a and O_b atomic charges, which become more negative in this phase, as shown in Figure 3d. OO breakage continues in phases 5 and 6 after the TS, and the finalization of OO bond cleavage takes place in phase 8 after the TS, denoted by a resisting contribution of the O_aO_b distance to the reaction path curvature (see Figure 3b) and by reaching the final OO distance of 2.8 Å in that phase (see Figure 3c).

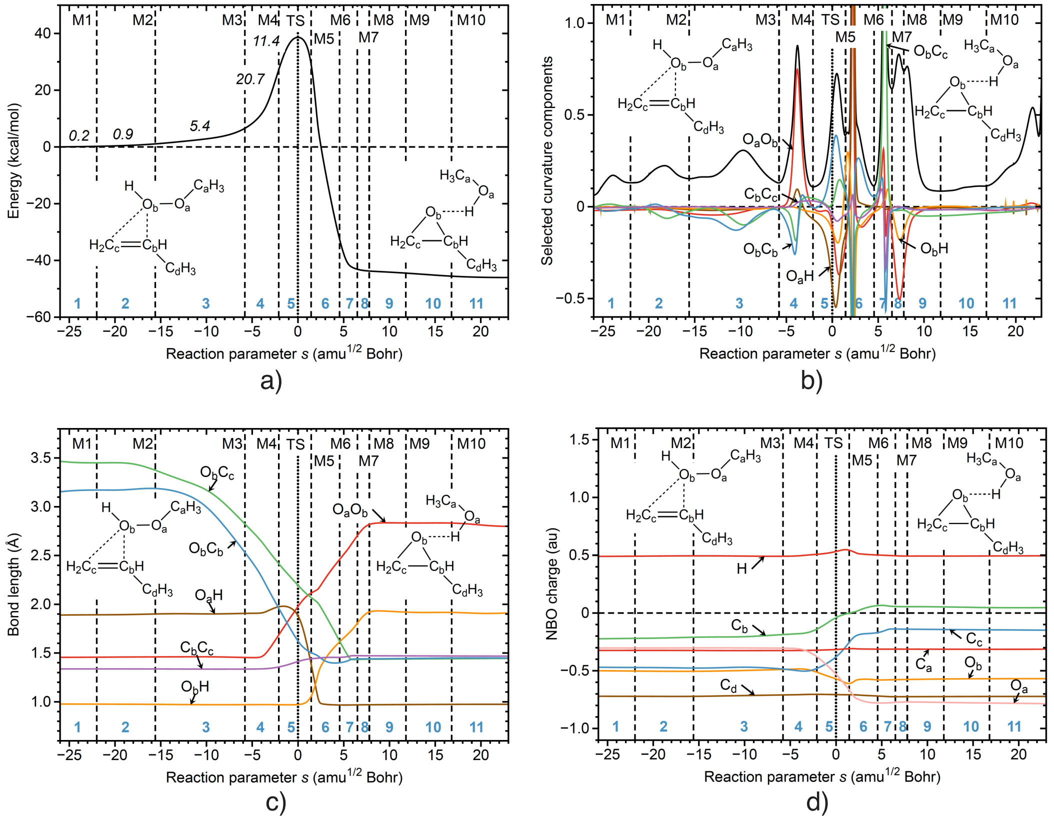

a) b) c) d)

Figure 3. Properties of reaction **R0** along the reaction path. (**a**) Energy profile, where the energy contributions of each reaction phase to the activation energy are indicated by italic numbers. (**b**) Decomposition of the reaction curvature into selected geometry components. (**c**) Change of selected bond lengths. (**d**) Change of selected NBO atomic charges. The curvature minima are shown as broken vertical lines and are labeled as M1, M2 and so on. The position of TS is indicated as a dotted line. The reaction phases are indicated by blue numbers. B3LYP/6-31G(d,p)/SDD(Ti) level of theory.

Although OO bond breakage continues in phases 5 and 6, the large curvature peaks in these phases are dominated by formation of the O_bC_b and O_bC_c bonds. The distances of both CO bonds continuously decrease from their starting values of 3.2 Å for O_bC_b and 3.5 Å for O_bC_c, respectively, with the steepest decline in phases 3 to 6, reaching their final values of 1.5 Å at the beginning of phase 7 (see Figure 3c), in line with the finalization of the CO epoxide bond formation indicated by large contributions of the O_bC_b and O_bC_c distances to the reaction path curvature in this phase. As of the asymmetric approach of the peroxide to the alcohol, the O_bC_b bond formation slightly preceeds the O_bC_c bond formation. The C_bC_c bond of the alcohol changes its character from a double bond to a single bond during the course of the epoxidation.

The corresponding CC bond elongation starts in the middle of phase 4, reaching its final value at the end of phase 7 (see Figure 3c) accompanied by a slight decrease of the negative C_b and C_c atomic charges, in line with the chemical concept that an sp^2 hybridized carbon atom is more electronegative than an sp^3 hybridized carbon atom (see Figure 3d). The C_bC_c distance contribution to the reaction path curvature in phases 4 to 7 (see a purple line in Figure 3b) is minor, reflecting that a change from double to single bond, i.e., a rehybriziation, requires less energy than that for bond breakage.

Interesting to note is the migration of the O_bH hydrogen atom from O_b to O_c during the epoxidation reaction (see reaction movie R0, Supplementary Materials), a unique feature of the non–catalyzed reaction, which starts before TS in phase 5 with a larger resisting contribution from the O_aH distance (see a brown line in Figure 3b) representing the necessary cleavage O_bH of the bond. The migration to O_a and formation of the new O_aH bond is finalized in phase 6 (see Figure 3c).

The energy profile in Figure 3a illustrates the energy contribution of each reaction phase to the total activation energy. The preparation phases 1 and 2 contribute with 1.1 kcal/mol and phase 3 where CO bond formation starts with 5.4 kcal/mol followed by phase 4 with the largest contribution of 20.7 kcal/mol, mainly resulting from OO bond cleavage with smaller contributions from CO bond formation. Phase 5 up to the TS adds another 11.4 kcal/mol, mainly from OH bond breakage with smaller contributions from CO bond formation. In the following sections, the catalyzed reactions are discussed with a focus on showing how the titanium catalyst changes the mechanism to lower the high activation energy of the non–catalyzed reaction, which is in the range of 40 kcal/mol, by almost 100%.

*Reaction **R1***: The dimeric titanium(IV)-catalyzed epoxidation reaction **R1** starts in the entrance channel from a van der Waals complex, where both the methyl–hydroperoxide and the allyl alcohol are coordinated to one of the Ti atoms leading to a hexacoordinate titanium environment, as depicted in Figure 2, with a TiO_b distance of 1.881 Å , a slightly longer TiO_a distance of 2.156 Å , and a TiO_c distance of 1.794 Å connecting the alcohol to the metal (see Table 4, showing that both the TiO_b as well as the TiO_c bonds are well in the range of the reference TiO single bond of TiOH with a TiO distance of 1.804 Å), whereas the TiO_a bond with the migrating oxygen atom is already elongated. (For comparison, the TiO bond distance of the TiO double bond of the TiO reference molecule is 1.612 Å) [174,175]. Selected reaction properties along the reaction path obtained from the URVA analysis of reaction **R1** are presented in Figure 4. The corresponding reaction movie R1 can be found in the Supplementary Material.

The overall curvature pattern resembles that for the non–catalyzed reaction **R0**. There are nine distinct reaction phases as shown in Figure 4b. Phases 1–2 are dominated by the rotation of the allylalcohol bringing the CC double in an optimal position for the interaction with the peroxide oxygen (see reaction movie R1, Supplementary Materials). In phases 3 and 4, CO bond formation starts (O_bC_b bond blue line and O_bC_c bond green line in Figure 4b) followed in phase 5 by the characteristic peak dominated by the start of OO bond breakage (red line in Figure 4b).

Although starting from a significantly larger distance than that found for reaction **R0** (3.8–4.2 Å compared with 3.1–3.5 Å, respectively) both CO bonds are finalized in phase 6 almost synchronously, which is reflected in the large curvature peak, with the O_bC_c bond formation being slightly ahead of the O_bC_b bond (see reaction movie R1, Supplementary Materials and Figure 4c) in line with the fact that the π lobe of the more electronegative C_c carbon is larger than that of the less electronegative C_b carbon –0.4 e versus –0.05 at the beginning of phase 6 see (Figure 4d). Furthermore, the change of the CC double bond to a CC single bond is finalized in this phase (purple line in Figure 4b).

As this happens after the TS, these events do not contribute to the energy barrier. As for the non–catalyzed reaction, the major chemical event contributing to the energy barrier is the cleavage of the peroxide OO bond. Interesting to note is that the starting OO distance is slight longer for reaction **R1** compared to reaction **R0** (1.467 Å versus 1.456 Å , respectively; see Table 4) and less covalent (H_ρ of –0.2034 Hr/Bohr^3 and –0.2187 Hr/Bohr^3, respectively), suggesting that the attachment to the Ti atom already weakens the OO bond. The TiO_a distance decreases in phase 4 from the original value of 2.156 Å to its final value of 1.779 Å reached at the end of phase 6 (see Figure 4c); this increasing TiO_a interaction also supports OO bond breakage.

Table 4. Bond length d, local mode force constant k^a and corresponding bond strength order BSO and energy density at the bond critical point H_ρ, for selected bonds of the reactant van der Waals complex, TS and product of the van der Waals complex for reactions **R0**–**R4**, investigated in this study. For atom labels, see the text and Figure 2. B3LYP/6-31G(d,p)/SDD(Ti) level of theory.

	Reactant				**TS**				**Product**			
Bond	**d**	$\mathbf{k^a}$	**BSO**	$\mathbf{H_\rho}$	**d**	$\mathbf{k^a}$	**BSO**	$\mathbf{H_\rho}$	**d**	$\mathbf{k^a}$	**BSO**	$\mathbf{H_\rho}$
	Å	**mDyn/Å**		**Hr/Bohr^3**	**Å**	**mDyn/Å**		**Hr/Bohr^3**	**Å**	**mDyn/Å**		**Hr/Bohr^3**
R0												
O_bO_a	1.456	3.939	0.966	−0.2187	1.977	0.377	0.230	0.0090	2.799	0.234	0.172	-
O_bC_b	3.148	0.066	0.054	-	1.623	0.273	0.141	−0.0980	1.449	3.575	0.807	−0.3029
O_bC_c	3.471	0.047	0.043	-	2.195	0.465	0.202	-	1.444	3.789	0.839	−0.3082
C_bC_c	1.337	9.507	1.935	−0.3846	1.413	4.903	1.144	−0.2994	1.469	5.307	1.218	−0.2305
O_bH	0.977	7.363	0.961	−0.5863	0.971	7.774	0.980	−0.6059	1.911	0.185	0.255	−0.0015
O_aH	1.889	1.352	0.522	-	1.882	0.109	0.210	-	0.974	7.445	0.965	−0.5828
R1												
O_bO_a	1.467	3.730	0.934	−0.2034	1.799	0.460	0.260	−0.0101	3.420	0.036	0.055	-
O_bC_b	4.259	0.024	0.027	-	2.171	0.150	0.094	-	1.425	4.063	0.880	−0.3437
O_bC_c	4.637	0.021	0.025	-	2.075	0.111	0.076	0.0012	1.449	3.667	0.821	−0.3008
C_bC_c	1.333	9.673	1.962	−0.3927	1.361	8.160	1.714	−0.3607	1.469	5.293	1.215	−0.2293
TiO_b	1.881	2.778	1.009	−0.0303	1.947	1.934	0.760	−0.0173	3.453	0.056	0.048	-
TiO_a	2.156	0.653	0.325	-	1.974	1.808	0.721	−0.0096	1.779	3.911	1.318	−0.0430
TiO_c	1.794	3.261	1.143	−0.0356	1.849	2.430	0.908	−0.0297	1.820	3.025	1.078	−0.0290
R2												
O_bO_a	1.468	3.677	0.926	−0.2017	1.827	0.478	0.266	−0.0052	3.576	0.031	0.050	-
O_bC_b	4.257	0.025	0.028	-	2.229	0.136	0.088	-	1.431	3.893	0.855	−0.3332
O_bC_c	3.846	0.011	0.016	-	2.013	0.166	0.100	−0.0040	1.439	3.917	0.858	−0.3179
C_bC_c	1.333	9.661	1.960	−0.3919	1.363	8.021	1.691	−0.3581	1.468	5.312	1.219	−0.2303
TiO_b	1.876	2.925	1.050	−0.0313	1.942	1.880	0.743	−0.0167	3.694	0.047	0.041	-
TiO_a	2.238	0.456	0.245	-	1.987	1.685	0.682	−0.0085	1.788	3.705	1.264	−0.0407
TiO_c	1.791	3.524	1.215	−0.0402	1.857	2.438	0.911	−0.0329	1.822	3.076	1.092	−0.0343
R3												
O_bO_a	1.468	3.661	0.924	−0.2012	1.812	0.420	0.246	−0.0079	3.600	0.026	0.045	-
O_bC_b	4.106	0.046	0.042	-	2.208	0.136	0.088	-	1.431	3.934	0.861	−0.3342
O_bC_c	3.552	0.028	0.030	-	2.062	0.148	0.093	−0.0003	1.441	3.871	0.851	−0.3147
C_bC_c	1.333	9.659	1.960	−0.3921	1.362	8.151	1.713	−0.3601	1.467	5.348	1.225	−0.2309
TiO_b	1.879	2.819	1.020	−0.0303	1.948	1.859	0.736	−0.0158	3.878	0.062	0.051	-
TiO_a	2.249	0.393	0.218	-	2.003	1.572	0.646	−0.0080	1.799	3.466	1.199	−0.0391
TiO_c	1.779	3.705	1.264	−0.0361	1.839	2.782	1.010	−0.0340	1.803	3.324	1.161	−0.0311
R4												
O_bO_a	1.469	3.658	0.923	−0.2005	1.808	0.440	0.253	−0.0080	3.866	0.016	0.033	-
O_bC_b	4.209	0.025	0.028	-	2.180	0.128	0.084	-	1.429	3.959	0.865	−0.3367
O_bC_c	3.780	0.011	0.016	-	2.077	0.124	0.082	0.0011	1.440	3.889	0.854	−0.3154
C_bC_c	1.332	9.710	1.968	−0.3934	1.361	8.211	1.723	−0.3611	1.467	5.367	1.229	−0.2314
TiO_b	1.877	2.861	1.032	−0.0308	1.962	1.654	0.672	−0.0142	4.031	0.042	0.038	-
TiO_a	2.258	0.380	0.213	-	1.989	1.673	0.678	−0.0098	1.795	3.554	1.223	−0.0397
TiO_c	1.785	3.644	1.247	−0.0390	1.844	2.732	0.995	−0.0336	1.808	3.386	1.178	−0.0352

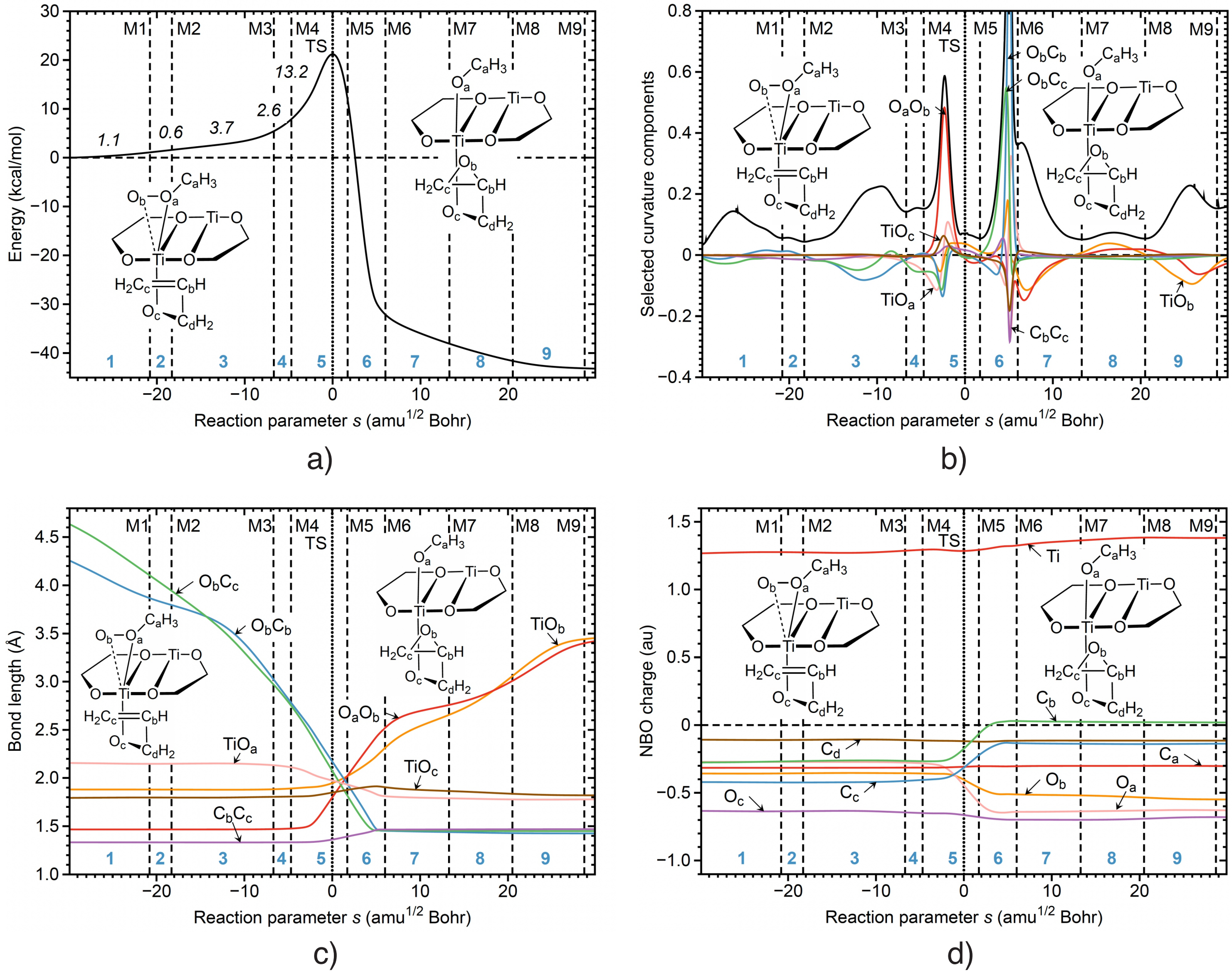

Figure 4. Properties of reaction **R1** along the reaction path. (**a**) The energy profile, where the energy contributions of each reaction phase to the activation energy are indicated by italic numbers. (**b**) Decomposition of the reaction curvature into selected geometry components. (**c**) The change of the selected bond lengths. (**d**) The change of the selected NBO atomic charges. The curvature minima are shown as broken vertical lines and are labeled as M1, M2 and so on. The position of TS is indicated as a dotted line. The reaction phases are indicated by blue numbers. B3LYP/6-31G(d,p)/SDD(Ti) level of theory.

In contrast to reaction **R0**, the final OO distance for reaction **R1**, although shorter (1.799 Å versus 1.977 Å, respectively), is reached at the end of the reaction in phase 9, synchronized with the elongation of the TiO_b distance (yellow line, Figure 4c). Another mechanistic difference between the non–catalyzed and catalyzed reaction is that instead of a hydrogen migration involving OH cleavage, which contributes to the same extent to the energy barrier as the later, the TiO_b bond has to be cleaved (the shorter of the two TiO bonds), and the O_b atom of the methyl–hydroperoxide has to be placed on top of the allylic C_bC_c double bond of the alcohol to initiate the attack of the CC double bond and the formation of the new O_bC_b and O_bC_c epoxide bonds.

The TiO_c distance remains fairly constant over the whole reaction (bond distance range between 1.794 and 1.820 Å; see Table 4), i.e., the alcohol is more or less fixed in the coordination sphere of the Ti atom, which makes the migration of the O_b easier and also guarantees stereoselectively. All three TiO bonds contribute to the reaction path curvature peak in phase 5 to some extent, however, less than the OH bond of the allyl alcohol in the non–catalyzed reaction.

Furthermore, breaking an OH bond is energetically more demanding than breaking a TiO bond [174,175]. A final interesting observation revealed in particular by the reaction movie R1 (Supplementary materials) is that the second Ti(DET) of the dimeric titanium catalyst does not become involved in the actual epoxidation reaction—its major role is to form the catalytic surface.

The energy contribution of each reaction phase to the total activation energy shown in the energy profile in Figure 4a provides further details on the energy balance of the catalyzed reaction **R1**. The preparation phases 1 and 2 contribute with 1.7 kcal/mol, followed by 6.3 kcal/mol in phases 3 and 4 mainly resulting from CO bond and cleavage with smaller contributions from TiO_a bond cleavage, which is substantially less than the 11.4 kcal/mol of phase reaction **R1** resulting dominantly for OH cleavage with smaller contributions from the CO bond formation.

The largest difference is, however, the contribution to the curvature peak being dominated by OO bond breakage, 13.2 kcal/mol versus 20.7 kcal/mol (catalyzed versus non–catalyzed). In summary, URVA reveals that the major activity of the dimeric titanium complex is the weakening of the OO bond to be broken, smoothly guiding the attacking peroxide oxygen atoms to the CC double of the alcohol and exchanging the expensive OH bond cleavage in the non-catalyzed reaction with TiO bond cleavage. In the following, the influence of the relative orientation of peroxide and alcohol on the dimeric titanium catalyst are further elucidated.

*Reaction **R2***: In reaction **R2**, the peroxide stays in the same position as in **R1**, i.e., above the surface spanned by the dimeric titanium catalyst, with the alcohol on the opposite side. However, the orientation of -CH_2 and the -CHCH−2O- parts of the allylalcohol is switched, thereby, positioning the -CH_2 parts to the inside of the catalyst (see Figure 2). As revealed by the curvature profile Figure 5b, the overall mechanism of reaction **R2** is similar to that of reaction **R1**.

There are 10 reaction phases, with one large curvature peak before the TS in phase 4, dominated by the start of OO bond breakage and with smaller contributions from the TiO bonds preceded by three phases orienting the dominated by the rotation of the allylalcohol bringing the CC double bond into an optimal position for interaction with the peroxide oxygen (see reaction movie R2, Supplementary Materials) and the start of the epoxide bond formation (O_bC_b bond blue line and O_bC_c bond green line in Figure 5b.) One reason for the shorter preparation (3 phases instead of four phases as for **R1**) is that whereas the starting O_bC_b distances are almost equal in both reactions (4.259 Å versus 3.846 Å for reactions **R1** and **R2**, respectively; see Table 4), the starting O_bC_c distance in reaction **R2** is considerably shorter (4.637 Å versus 4.257 Å for reactions **R1** and **R2**, respectively; see Table 4 and Figure 5c).

This leads to a more asynchronous finalization of the epoxide bonds in reaction **R2** as reflected in two distinct curvature peaks; one in phase 5 dominated by the O_bC_c bond followed by a separate peak in phase 6 dominated by the O_bC_b bond (see Figure 5b). However, these events take place after TS as with reaction **R1**, i.e., they do not affect the energy barrier, which is reflected in the similar activation energies (21.2 and 22.6 kcal/mol, for **R1** and **R2**, respectively).

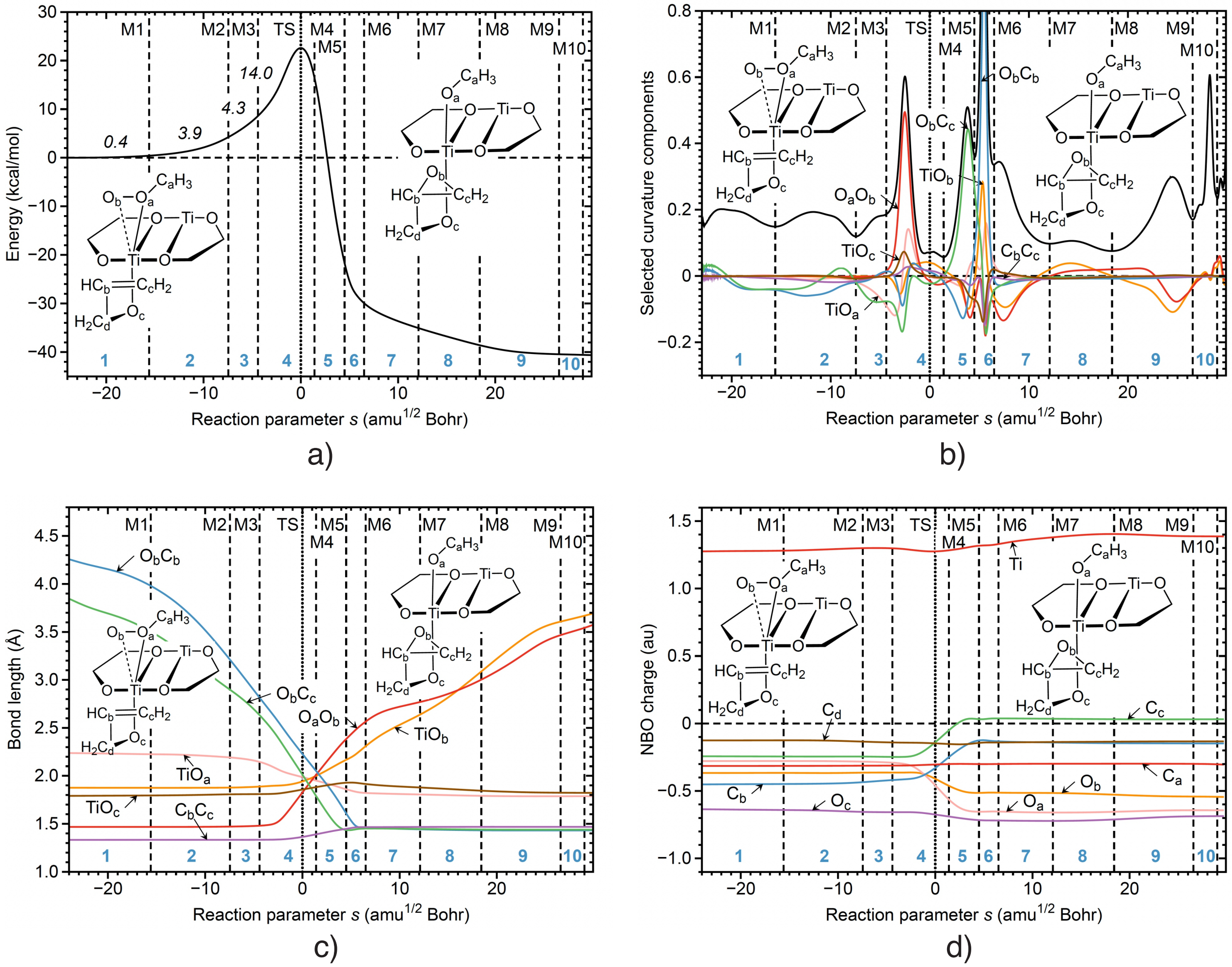

a)

b)

c)

d)

Figure 5. Properties of reaction **R2** along the reaction path. (**a**) The energy profile, where the energy contributions of each reaction phase to the activation energy are indicated by italic numbers. (**b**) Decomposition of the reaction curvature into selected chemical bonds. (**c**) The change of the selected bond lengths. (**d**) The change of the selected NBO atomic charges. The curvature minima are shown as broken vertical lines and are labeled as M1, M2 and so on. The position of TS is indicated as a dotted line. The reaction phases are indicated by blue numbers. B3LYP/6-31G(d,p)/SDD(Ti) level of theory.

Reaction ***R3***: In reaction **R3**, the allylalcohol is oriented as in reaction **R1**, i.e., with the -CH_2 group to the outside of the catalyst; however, the peroxide and the allylalcohol switch sides, now with the allylalcohol above the surface spanned by the dimeric titanium catalyst and the peroxide below (see Figure 2). Again, the overall mechanism of the epoxidation reaction is the same as for reactions **R1** and **R2**, as shown by the reaction profile in Figure 6b. Being placed above the surface spanned by the dimeric titanium catalyst makes it easier for the allylacohol to rotate into the best position for the interaction with the peroxide oxygen (see movie R3 of the Supplementary Material).

Both epoxide CO distances at the start of the reaction are with 4.106 Å for O_bC_b and 3.552 Å for O_bC_c found to be the shortest of all four reactions, which is reflected by the fact that the preparation phases of the reaction **R3** contribute to only 4.5 kcal/mol to the energy barrier (see Figure 5a) compared to an energy contribution of 8.0 and 8.6 kcal/mol for reactions **R1** and **R2**, respectively. This leads to the overall smallest energy barrier of 22.3 kcal/mol found for all four reactions, although the contribution to the start of the

OO bond breaking is with 15.1 kcal/mol higher than that for **R1** and **R2** with 13.2 and 14.0 kcal/mol, respectively.

The finalization of the O_bC_c and O_bC_b epoxide bonds occurs for reaction **R3** less synchronously than for reaction **R1** although the O_bC_c bond is finalized in phase 6 and the O_bC_b bond in phase 7 (see Figure 6b), in line with the changes of the corresponding bond lengths (see Figure 6c) and changes of the corresponding atomic charges (see Figure 6d).

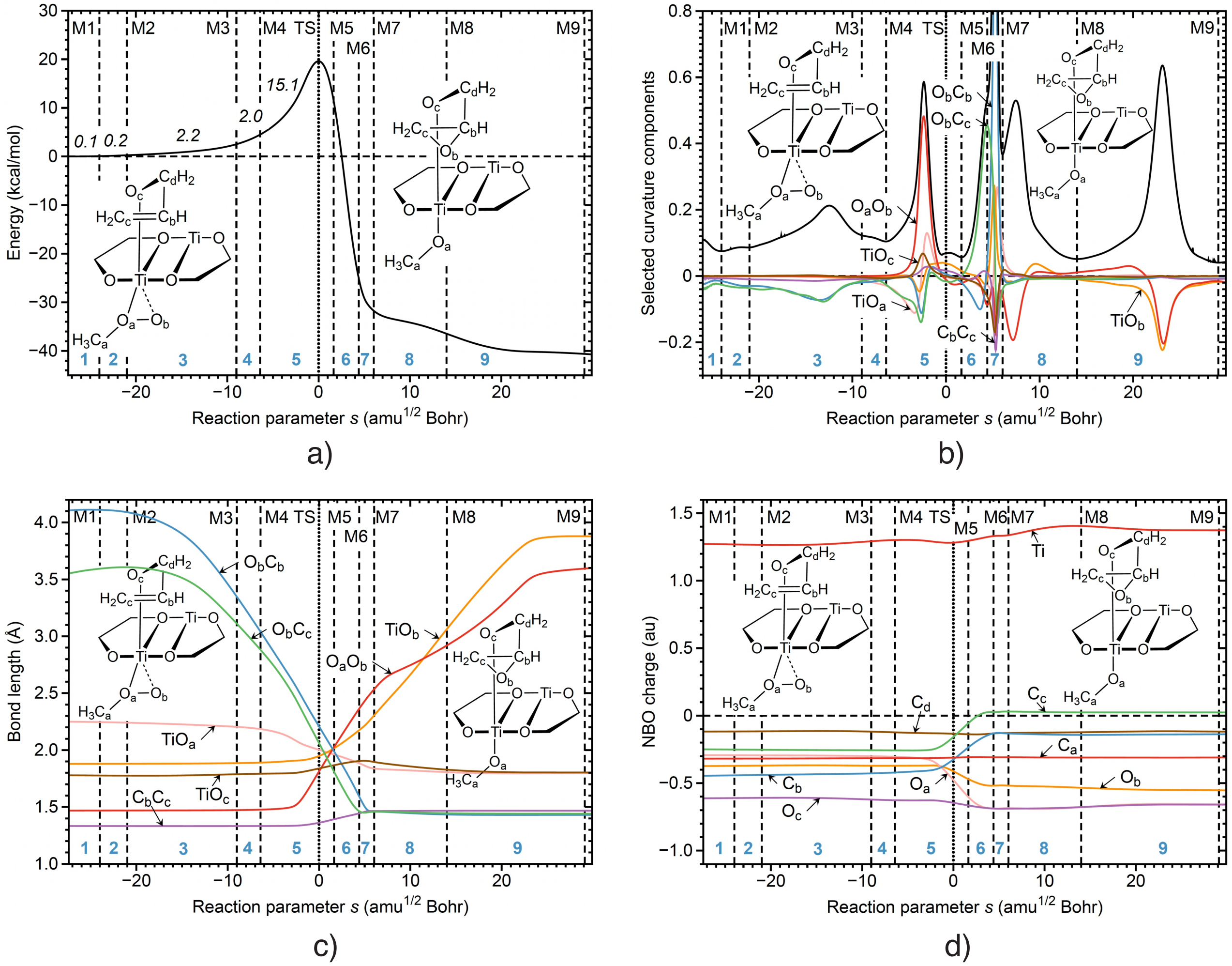

a) b)

c) d)

Figure 6. Properties of reaction **R3** along the reaction path. (**a**) The energy profile, where the energy contributions of each reaction phase to the activation energy are indicated by italic numbers. (**b**) Decomposition of the reaction curvature into selected chemical bonds. (**c**) The change of the selected bond lengths. (**d**) The change of the selected NBO atomic charges. The curvature minima are shown as broken vertical lines and are labeled as M1, M2 and so on. The position of TS is indicated as a dotted line. The reaction phases are indicated by blue numbers. B3LYP/6-31G(d,p)/SDD(Ti) level of theory.

Similarly to reactions **R1** and **R2**, the C_bC_c bond is changing its character from double to single bond between phases 5 and 7, and the TiO_b bond cleavage starts in phase 5, which is shown in Figure 6b–d. Interesting to note are the two large curvature peaks in phases 8 and 9 being dominated by the finalization of OO and TiO_b bond breakage accompanied by the rotation of the peroxide into its final position. These two peaks are more pronounced as for the reactions **R1** and **R2** in line with the increasing final distances OO distances (3.420 Å for reaction **R1**, 3.694 Å for reaction **R2** and 3.600 Å for reaction **R3**, respectively) and the final TiO_b distances (3.453 Å for reaction **R1**, 3.576 Å for reaction **R2** and 3.878 Å for reaction **R3**, respectively).

However, since these events happen after the TS, these differences do not influence the reaction barrier. Interesting to note is that the catalyzed OO bond breakage appears to occur in two distinct steps (i.e., *quasi-quantized*) in contrast to the non–catalyzed reaction with an almost linear increase of the OO distance, which we have also observed for other catalyzed reactions [72].

*Reaction **R4***: This reaction is the counterpart to reaction **R3** with the -CH_2 group to the inside of the catalyst. The reaction profile is similar to that of the reaction **R3** (see Figure 7b) indicating switching the position of the -CH_2 group to the inside of the catalyst does not have a major mechanistic influence. There is one different nuance right at the beginning of the reaction; starting with distances of 4.209 Å for O_bC_b and 3.780 Å for O_bC_c at the beginning of the reaction, both CO distances first increase in phase 2 (see Figure 7c) in line with a pronounced curvature peak being dominated by a resisting contribution of both OC bonds (see Figure 7b) although the contribution of this phase to the activation energy is with 0.5 kcal/mol only minor.

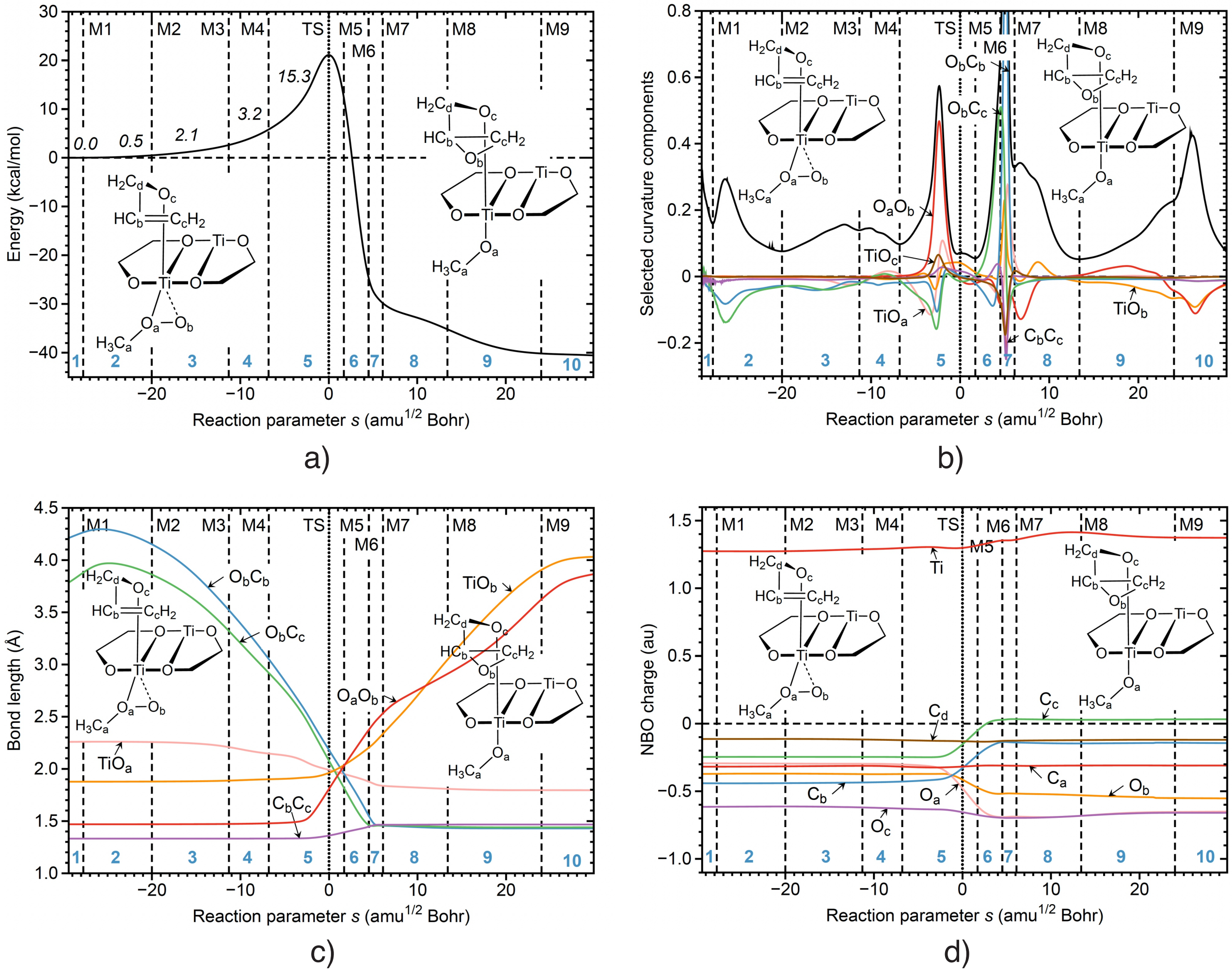

a)

b)

c)

d)

Figure 7. Properties of reaction **R4** along the reaction path. (**a**) The energy profile. (**b**) Decomposition of the reaction curvature into selected chemical bonds. (**c**) The change of the selected bond lengths. (**d**) The change of the selected NBO atomic charges. The curvature minima are shown as broken vertical lines and are labeled as M1, M2 and so on. The position of TS is indicated as a dotted line. The reaction phases are indicated by blue numbers. B3LYP/6-31G(d,p)/SDD(Ti) level of theory.

The total contribution of the preparation phases 1–4 to the activation energy is 5.8 kcal/mol and that of phase 5 dominated by the start of OO bond breaking 15.3 kcal/mol of the activation energy (see Figure 7a) summing up to the second largest barrier of 22.5 kcal/mol. Similarly for reaction **R3**, the finalization of the O_cC_b and O_bC_b bonds formation in reaction **R4** takes place almost synchronously, with the O_bC_c bond being finalized in phase 6 and the O_bC_b bond being finalized in phase 7 (see Figure 7b).

The C_bC_c bond changes its character between phases 5 and 7, and the TiO_b bond starts to break in phase 5 of the reaction, which is confirmed in Figure 7b–d. As suggested by the reaction movie R4 (Supplementary Materials) and the smaller curvature peaks in phases 8–10, the final breakage of the OO and TiO_b bonds seems to be easier in reaction **R4** with the smaller -CH_2 group on the inside of the catalyst, also facilitating the rotation of the epoxide group into its final position in the product van der Waals complex.

In summary, as revealed by URVA, the chemical event mainly responsible for the activation energy is the cleavage of the peroxide OO bond and in second order, the start of CO epoxide bond formation accompanied by changes of the TiO bonds for the catalyzed reactions **R1**–**R4** and changes of the OH bond and hydrogen migration for the non-catalyzed reaction **R0**. The actual rehybridization of target carbon atoms from sp^2 to sp^3 occurs after the transition state, which does not require energy. Different orientations of the reactants on the quasi-surface spanned by the dimeric titanium(IV) catalyst affect the reaction mechanism only marginally. In the next section, the URVA results are complemented by a comprehensive bond strength analysis of all bonds involved in the epoxidation process, performed at all stationary points of reactions **R0**–**R4**.

3.3. Chemical Bond Analysis

This section is devoted to the bond properties of the methyl–hydroperoxide OO bond (O_aO_b) to be broken, the CC (C_bC_c) double bond of allylalcohcol transforming into a CC single bond in the final epoxide, the two new CO epoxide bonds (O_bC_b, O_bC_c) and the three TiO bonds (TiO_a,TiO_b,TiO_c), evaluated at the stationary points of reactions **R0**–**R4** (i.e., reactant van der Waals complex, TS, product van der Waals complex; sketches of the TSs are shown in Figure 8).

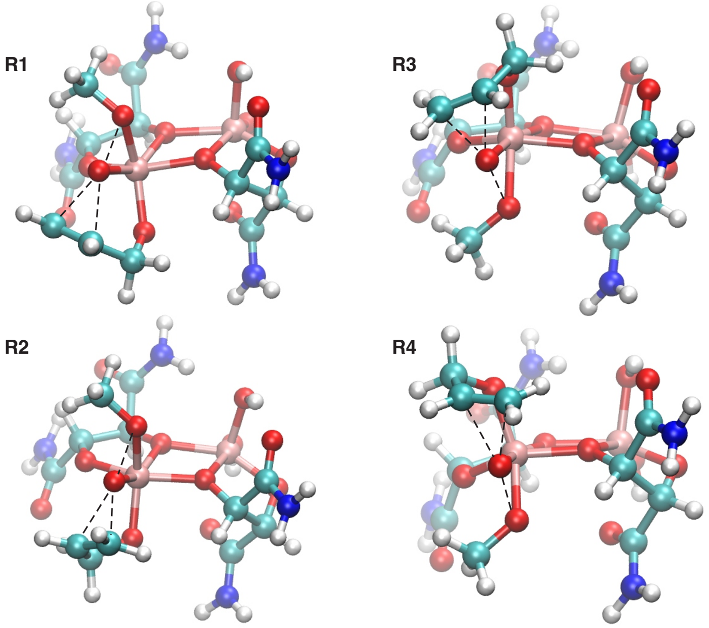

Figure 8. Transition state structures of the catalyzed epoxidation reactions between methyl–hydroperoxide and allylalcohol (**R1**–**R4**) studied in this work.

For the non-catalyzed reaction **R0,** instead of the TiO bonds, the corresponding OH bonds (O_bH and O_aH; see Figure 2) are analyzed. The bond properties discussed in this section include bond lengths *d*, intrinsic bond strengths based on local mode force constants k^a and associated BSOs, complemented with the energy density at the bond critical point H_ρ assessing the covalent character of the bonds. The results are summarized in Table 4, and in Figures 9–12, general trends and correlations between these properties are illustrated.

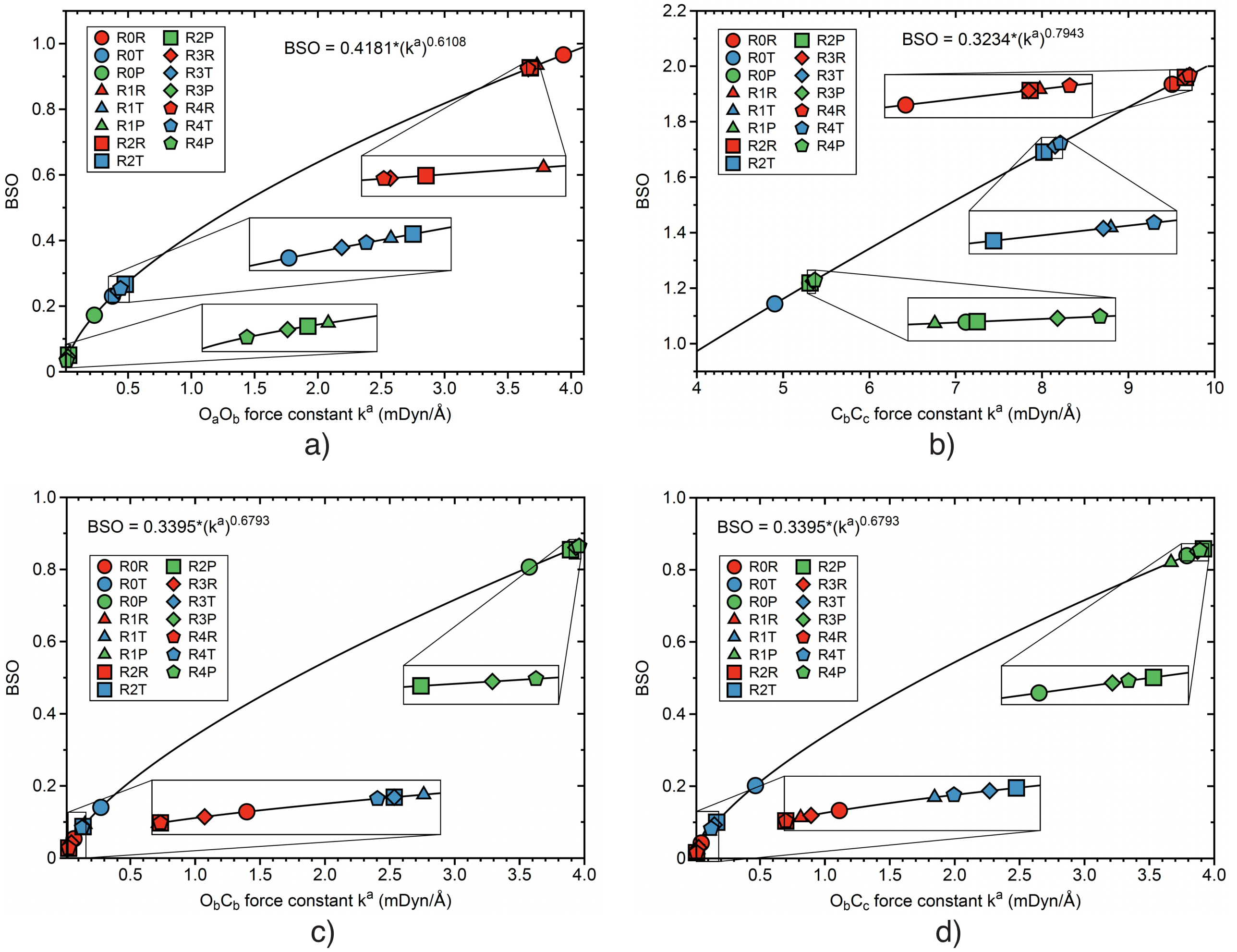

a) b) c) d)

Figure 9. BSO as a function of k^a. (**a**) OO bonds, (**b**) CC bonds, (**c**) O_bC_b and (**d**) O_bC_c epoxide bonds (for atom labels, see text). RnR, RnT and RnP indicate the reactant (red color), TS (blue color) and product (green color) for reactions **Rn**, with n=0,· · · 4. B3LYP/6-31G(d,p)/SDD(Ti) level of theory.

OO bonds: Figure 9a shows the BSO values of the OO bonds calculated from the corresponding local mode force constants k^a(OO) utilizing the power relationship described above. The strongest OO bonds are found for the reactant complexes (red points) with the overall strongest reactant OO bond for the non-catalyzed reaction **R0**. The weakest OO interactions are found for the product complexes (green points). The bond strength of the TS OO bonds (blue points) is closer to that of the products, i.e., at the TSs, the most substantial part of OO bond breakage is achieved in line with the URVA result that OO bond breakage is the major chemical event accounting for the activation energy.

Figure 9a and Table 4 data reflect that the reactant van der Waals complex of the non-catalyzed reaction **R0** has the strongest OO bond of all five reactants investigated in this work, (k^a(OO) values of 3.939, 3.730, 3.677, 3.661 and 3.658 mDyn/Å, for reactions **R0**–**R4** and corresponding BSO values of 0.966, 0.934, 0.926, 0.924 and 0.923, respectively). The

H_ρ(OO) value of the OO reactant bond of reaction **R0** is more negative (–0.2187 Hr/Bohr^3) than the corresponding values for the catalyzed reactions **R1**–**R4** (–0.2034, –0.2017, –0.2012 and –0.2005 Hr/Bohr^3, respectively), indicating the more covalent character of the non–catalyzed reactant OO bond; see also Figure 11a, which shows the correlation between H_ρ and k^a for reactants and TSs.

For the products, no OO bond critical point was found. These results are in perfect agreement with the URVA trends found for the contribution of OO bond cleavage to the activation energy discussed above (20.7 kcal/mol for **R0**, compared with 13.2, 14.0, 15.1 and 15.3 kcal/mol, for **R1**–**R4**, respectively).

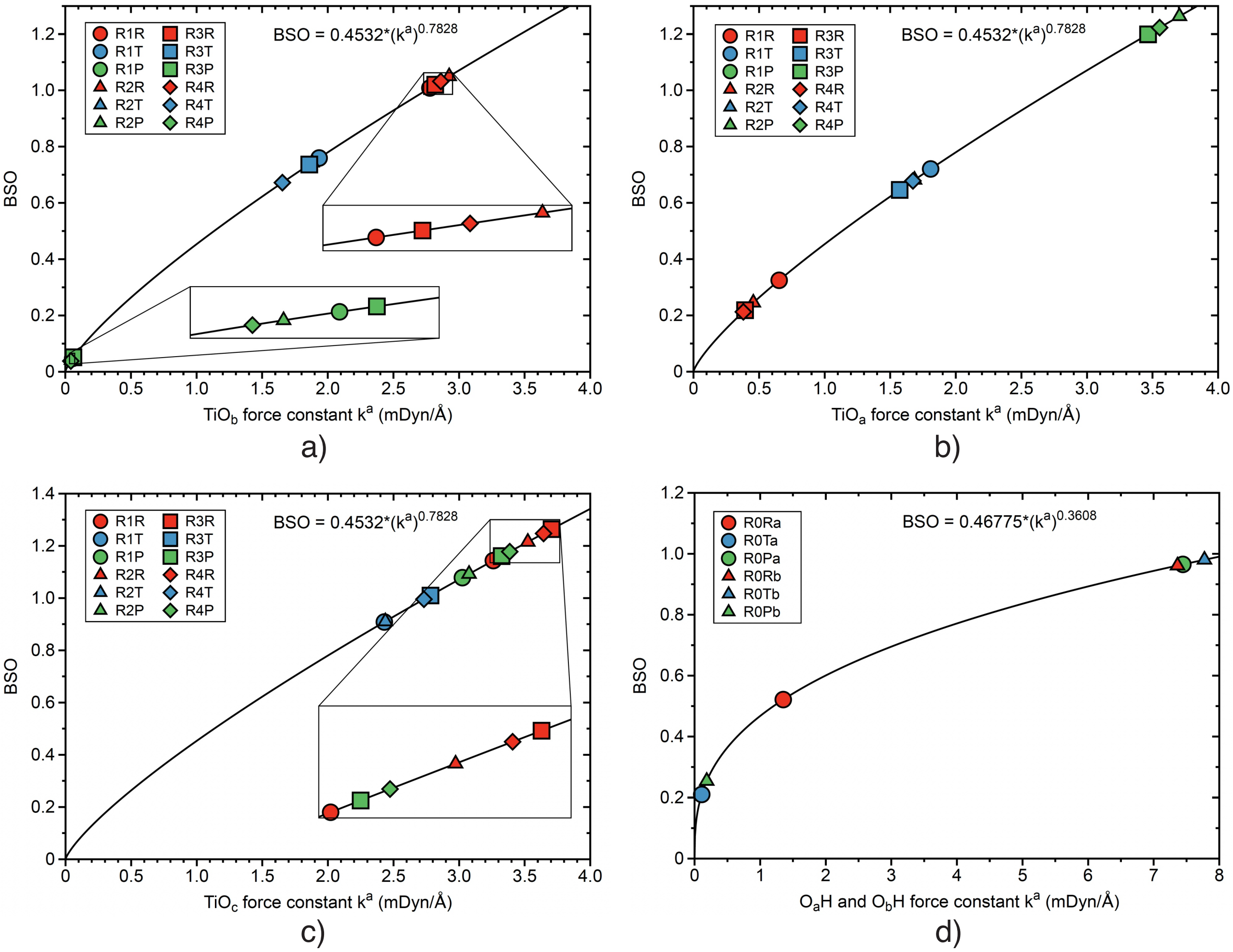

Figure 10. BSO as a function of k^a. (**a**–**c**) TiO_b, TiO_a and TiO_c bonds (**d**) O_aH and O_bH bonds (for atom d labels see text). RnR, RnT and RnP indicate the reactant (red color), TS (blue color) and product (green color) for reactions **Rn**, with n=0,$\cdots$4. B3LYP/6-31G(d,p)/SDD(Ti) level of theory.

Interesting to note is the different OO bond strength decay at the TSs for non-catalyzed versus catalyzed reactions, clearly resulting from the fact that the overall mechanism for the non–catalyzed and catalyzed reaction is quite different and so are the TSs structures as depicted in Figure 8. For reaction **R0**, the OO bond breaking process is most advanced at the TS with a d(OO) value of 1.977 Å and a BSO of 0.230 compared to d(OO) values of 1.799, 1.827, 1.827 and 1.808 Å and BSO values of 0.260, 0.266, 0.246 and 0.253 for **R1**–**R4**, respectively, (see Table 4). As revealed by the H_ρ values, at the TSs, the OO bond no longer has a covalent character for all five reactions.

In the case of the product van der Waals complexes, there is still some weak OO interaction for the non-catalyzed reaction **R0** (d(OO) = 2.799 Å and BSO = 1.72, respectively, compared to close to the zero OO interaction in the catalyzed reactions with d(OO) distances larger than 3.4 Å and BSO values less than 0.055. As shown in Figure 13 correlating k^a(OO) and d(OO), there is some trend (R^2 = 0.9372) that the shorter OO bond is also stronger.

CC bonds: Figure 9b shows the bond order changes during the transformation of the CC double of the reactant allylalcohol into the CC single bond of the epoxide product. Reactant BSO(CC) values are close to 2 (red points), and product BSO(CC) values are close to 1.2 (i.e., typical values for CC epoxide bonds, which are generally somewhat stronger than aliphatic CC single bonds [176,177]). TS BSO (CC) values are in the range of 1.7, i.e., closer to the reactant values in line with the URVA results that the finalization of CC bond lengthening occurs after the TS.

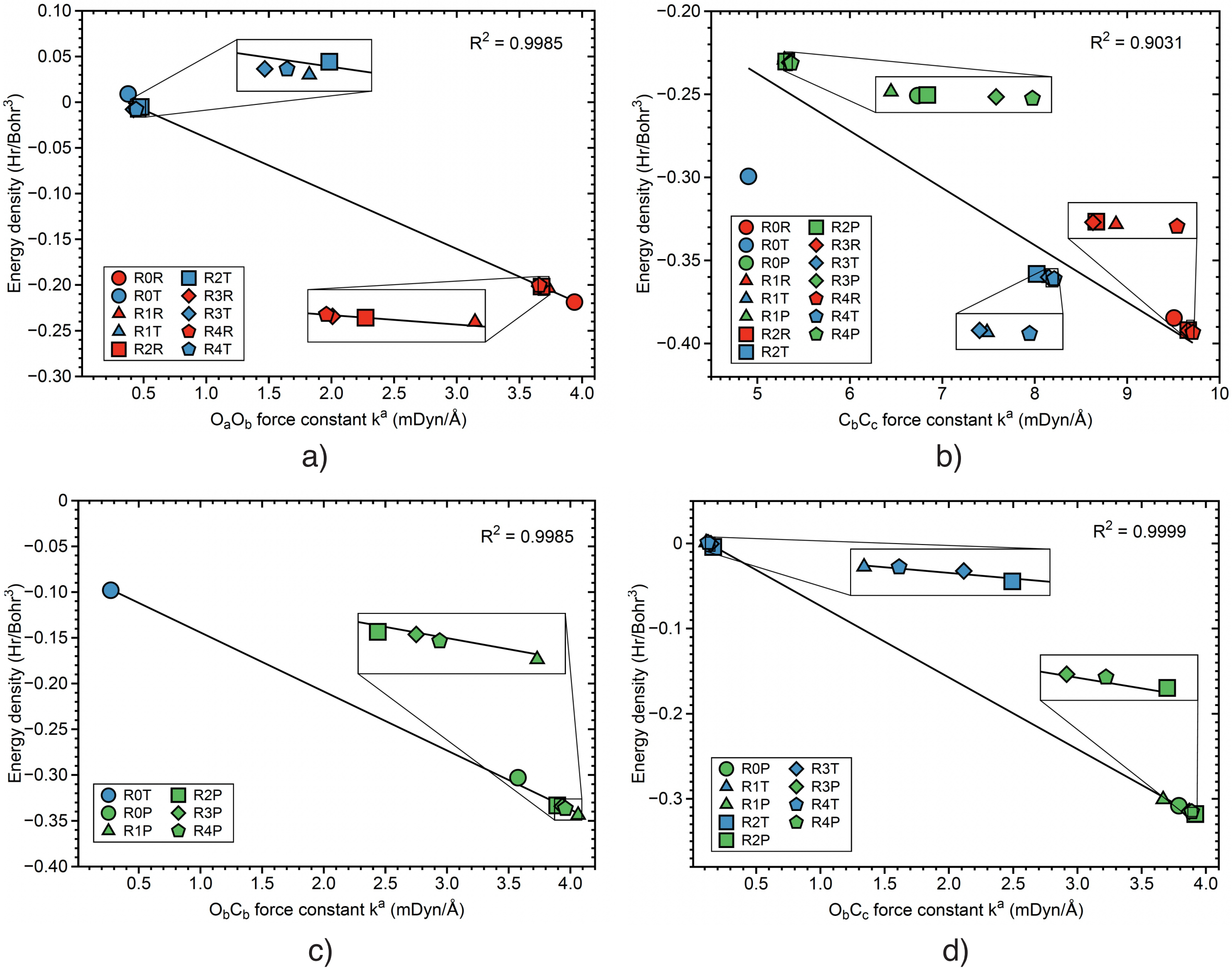

a)

b)

c)

d)

Figure 11. Correlation between energy density and local mode force constant. (**a**) OO bond, (**b**) CC bond, (**c**) O_bC_b bond and (**d**) O_bC_c bond. RnR, RnT and RnP indicate the reactant (red color), TS (blue color) and product (green color) for reactions **Rn**, with n=0,· · · 4. B3LYP/6-31G(d,p)/SDD(Ti) level of theory.

There is one distinct outlier in Figure 9b, the TS of the non–catalyzed reaction, which not only lies outside the TS cluster but also has the weakest CC bond (BSO = 1.144) of all CC bonds investigated in the work, which again is a result of the unique TS structure of the non–catalyzed reaction **R0**, (see also Figure 8.) As depicted by the data in Table 4 the

CC bond strength of the reactant of **R0** is with k^a(CC) = 9.507 mDyn/Å and BSO = 1.935 close to the values found for the catalyzed reactions **R1**–**R4** (k^a(CC) values of 9.673, 9.661, 9.659 and 9.710 mDyn/Å, respectively, and BSO values of 1.935, 1.962, 1.960 and 1.968, respectively).

The same holds for the CC bond strength of the products, which are with k^a(CC) = 5.307 mDyn/Å and BSO = 1.218 close to the values found for the catalyzed reactions **R1**–**R4** (k^a(CC) values of 5.293, 5.312, 5.348 and 5.367mDyn/Å, respectively, and BSO values of 1.215, 1.219, 1.225 and 1.229, respectively).

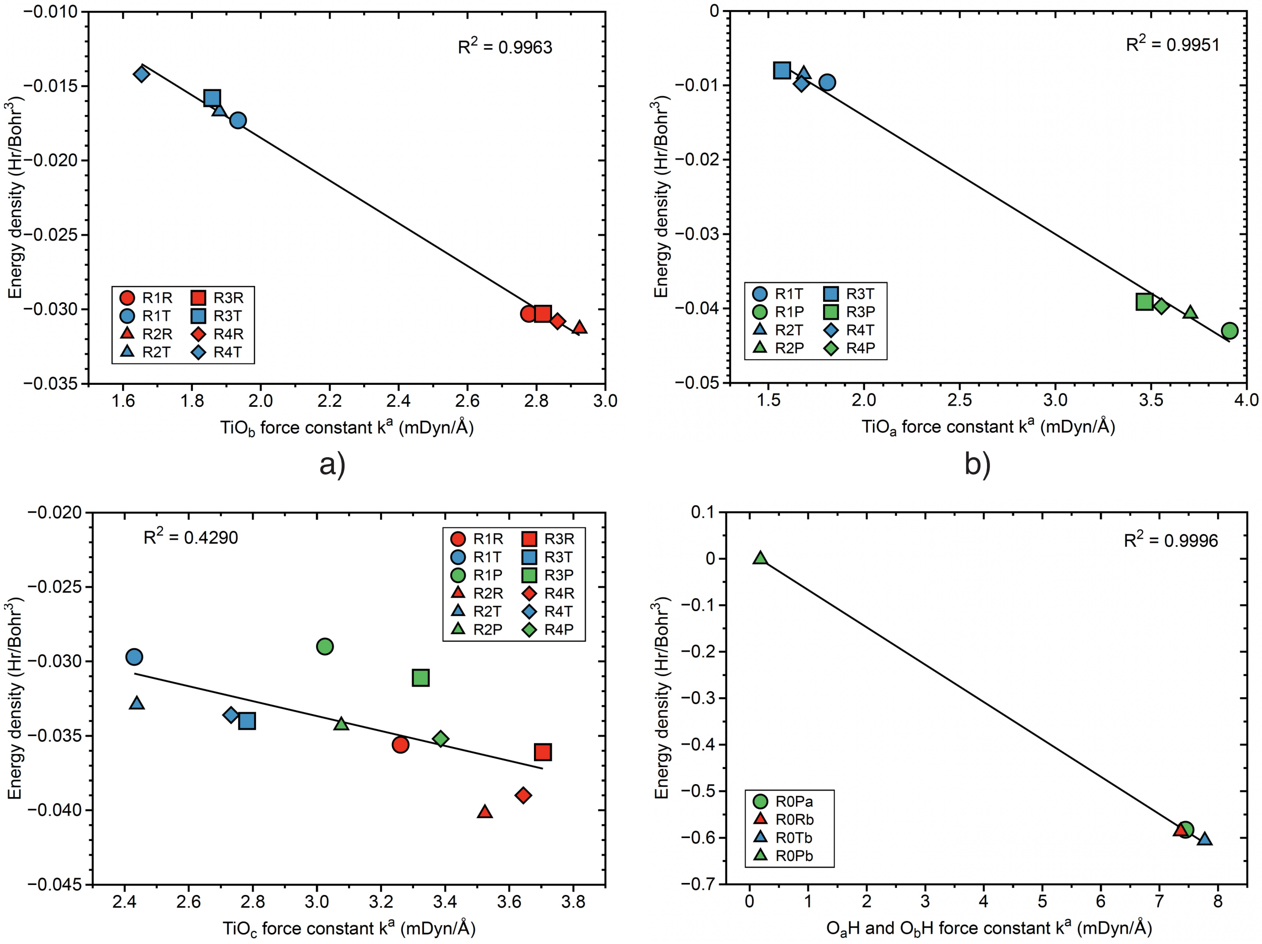

a) b)

c) d)

Figure 12. Correlation between energy density and local mode force constant. (**a**–**c**) TiO_b, TiO_a and TiO_c bonds and (**d**) O_aH and O_bH bonds. RnR, RnT and RnP indicate the reactant (red color), TS (blue color) and product (green color) for reactions **Rn**, with $n=0,\cdots 4$. B3LYP/6-31G(d,p)/SDD(Ti) level of theory.

However, this is no longer true for the TS; k^a(CC) = 4.903 mDyn/Å and BSO = 1.114 for reaction **R0** compared to k^a(CC) values of 8.16, 8.021, 8.151 and 8.211 mDyn/Å, respectively, and BSO values of 1.714 1.691, 1.713 and 1.723, respectively, for reactions **R1**–**R4**. This is also reflected in the energy density values. The TS H_ρ(CC) value of **R0** is with a value of –0.2994 Hr/Bohr^3 much smaller than those for reactions **R1**–**R4** (–0.3607, –0.3581, –0.3601 and –0.3611 Hr/Bohr^3, respectively; see also Figure 11b). This illustrates that local mode force constants are very sensitive to the electronic structure environment of the bond under consideration [73].

In the non–catalyzed reactant, both carbon atoms C_b and C_c are sp^2 hybridized, while in the product, both adapt a hybridization close to sp^3, which is typical for three-membered rings [177–179], with a TS hybridization in between. The O_b atom is more or less equally centered over the CC bond in the TSs of the catalyzed reactions, as reflected in the O_bC_b and O_bC_c distance pairs of 2.171 and 2.075 Å, 2.229 and 2.013 Å, 2.208 and 2.062 Å as well as 2.180 and 2.077 Å, respectively, for **R1**–**R4**, being slightly closer to C_c.

In the TS of the non–catalyzed reaction, the O_b atom is much closer to the C_b atom (1.623 and 2.195 Å) leading to a more unbalanced change of the hybridization (i.e, the C_c carbon keeps its initial hybridization sp^2 longer, while the C_b carbon changes its hybridization quicker to sp^3, because of the stronger interaction O_b and, as such, to an unbalanced electron density distribution as reflected in the local mode force constant.

Interesting to note is that this is not seen in the corresponding CC bond lengths d(CC) of 1.337 Å, 1.413 Åand 1.469 Å for the reactant, TS and product) showing a normal trend as also reflected in Figure 13b. In this regard, the CC bond of the TS of the non–catalyzed reaction **R0** is another example that the shorter bond is not always the stronger bond [96,97,99,110,112,180,181].

CO bonds: There are two new epoxide CO bonds formed during the epoxidation reaction. Figure 9c,d show the BSO values for the O_bC_b and the O_bC_c bonds, respectively. In both cases, there are three clusters of points. The strongest CO bonds are found for the products (in green) with very weak, almost zero interactions for the reactants (read points) and with the TS cluster (blue) close to the reactant cluster, confirming the URVA results that CO bond formation starts before the TS and, as such, contributes in second order to the reaction barriers, whereas the actual finalization of these bonds occurs well after the TS.

The overall pattern is the same for both graphs with two clear differences, (1) the TS O_bC_c bond (Figure 9d) and (2) the product O_bC_c bond (Figure 9c) of reaction **R0** are somewhat separated from the corresponding clusters of the catalyzed reactions, reflecting the (i) different approach mechanism of the attacking peroxide oxygen, which, as discussed above, leads to a different TS topology and (ii) the different epoxide product formed.

As shown in Table 4, the product CO bonds of reaction **R0** have $k^a(O_bC_b)$ = 3.575 mDyn/Å and BSO = 0.807 and $k^a(O_bC_c)$ = 3.789 mDyn/Å and BSO = 0.839, i.e., the O_bC_c is slightly stronger than the O_bC_b bond. The corresponding values for the catalyzed reactions **R1**–**R4** are: $k^a(O_bC_b)$ = 4.063 mDyn/Å and BSO = 0.880, $k^a(O_bC_c)$ = 3.667 mDyn/Å and BSO = 0.821; $k^a(O_bC_b)$ = 3.893 mDyn/Å and BSO = 0.855, $k^a(O_bC_c)$ = 3.917 mDyn/Å and BSO = 0.858; $k^a(O_bC_b)$ = 3.934 mDyn/Å and BSO = 0.861, $k^a(O_bC_c)$ = 3.871 mDyn/Å and BSO = 0.851; and $k^a(O_bC_b)$ = 3.959 mDyn/Å and BSO = 0.865, $k^a(O_bC_c)$ = 3.889 mDyn/Å and BSO = 0.0.854, respectively.

For reaction **R2**, as for **R0**, the (O_bC_b) is slightly stronger, whereas for **R1**, **R3** and **R4**, the (O_bC_c) is the stronger bond. Smaller bond strength differences between (O_bC_b) and (O_bC_c) relate to a more synchronous formation of both bond. Again, in this regard, the local mode force constants are a sensitive tool monitoring the different electronic environment caused by the different orientation of the peroxide and allylalcohol on the catalyst. Figure 11c,d show the corresponding $H_\rho(O_bC_b)$ versus $k^a(O_bC_b)$ and $H_\rho(O_bC_c$ versus $k^a(O_bC_c)$ correlations, where the high R^2 values are somewhat misleading because they result from a smaller dataset.

No bond paths were found for the reactants or even for some of the TSs; see Table 4. As reflected in the bond length versus bond strength plots (see Figure 13c,d), there is a trend that the shorter CO bonds are also the stronger bonds with moderate R^2 values of 0.8666 and 0.8884, respectively, mainly deteriorated by the non–catalyzed reaction **R0**.

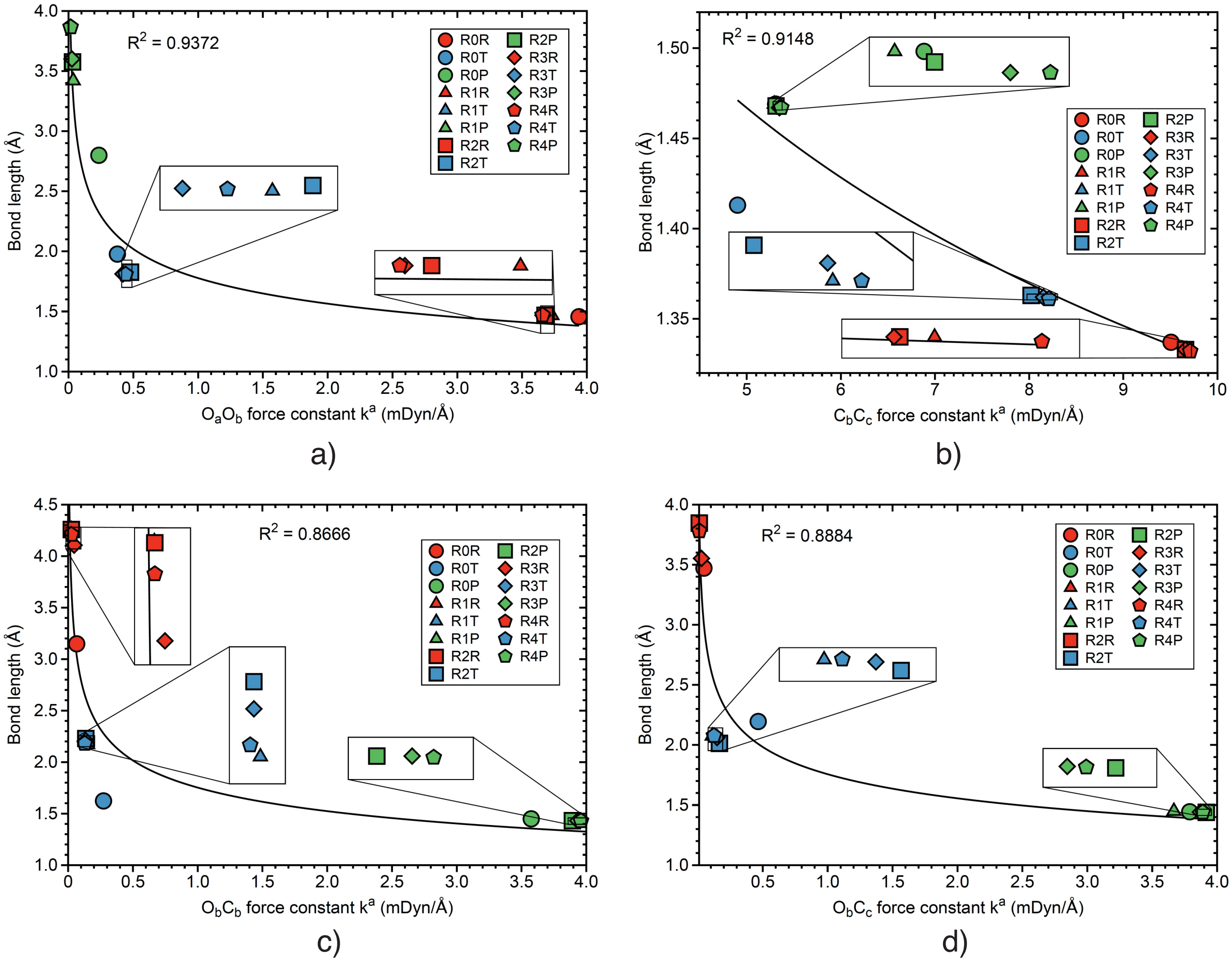

Figure 13. Correlation between bond lengths and local mode force constants. (**a**) OO bond, (**b**) CC bond, (**c**) O_bC_b bond and (**d**) O_bC_c bond. RnR, RnT and RnP indicate the reactant (red color), TS (blue color) and product (green color) for reactions **Rn**, with n=0,$\cdots$4. B3LYP/6-31G(d,p)/SDD(Ti) level of theory.

TiO bonds: The catalyzed epoxidation reactions **R1**–**R4** involve three TiO bonds: TiO_a, which coordinates the OCH_3 part of the methyl–hydroperoxide; TiO_c, which coordinates the OCH_2 part of the allylalcohol; and mechanistically the most important TiO_b, coordinating the O_b atom of the peroxide transferred to the CC double bond of allylalcohol for the epoxide bond formation (see Figure 2). The different roles of these TiO bonds are reflected in the different BSO patterns shown in Figure 10a–c. TiO_c bonds can be considered as *spectator* bonds fixing the allylalcohol during the epoxidation reaction.

This is reflected by smaller variations in the bond strength (see Figure 10c), stronger bonds with BSO values ranging from 1.143 to 1.264 for reactants (red points), slightly weaker bonds with BSO values between 1.078 and 1.178 for products (green points) and the TSs with BSO values between 0.908 and 1.010, without distinct cluster formation. As depicted in Figure 11c, there is no correlation between $H_\rho(TiO_c)$ and $k^a(TiO_c)$. Bond length changes $d(TiO_c)$ are small, varying only between 1.78 and 1.86 Å (see Figure 14c). Figure 14a,b show the BSO curves for TiO_b and TiO_a, respectively. As seen before for OO and CO bonds, there are three clusters of points corresponding to reactants (red points), TSs (blue points) and products (green points).

As notable from these plots, the strength of the TiO_b and TiO_a reactant and product bonds change during the epoxiation reaction in a complementary way, i.e., there are only weak TiO_b interactions in the product, with the two O_bC_b and O_bC_c bonds fully developed and stronger TiO_b bonds in the reactants. On the contrary, there are stronger TiO_a bonds in the products with the OCH_3 part the methyl–hydroperoxide fully coordinated and weaker and longer TiO_b bonds in the reactants (see also Figure 14a,b) facilitating TiO_b bond breaking and the move of O_b towards the CC double bond.

The same complementarity is also shown in the energy density plots Figure 12a,b where it has to be considered that no bond critical points were found for the product TiO_a bonds and for the reactant TiO_b bonds, respectively. Interesting to note is that the TiO_a and TiO_b bonds at the TS are of similar strength and covalent character, as reflected in the data in Table 4 and the corresponding plots. This all shows that the Sharpless catalyst does much more than weakening the OO bond to be broken. It carefully orchestrates the whole epoxidation event.

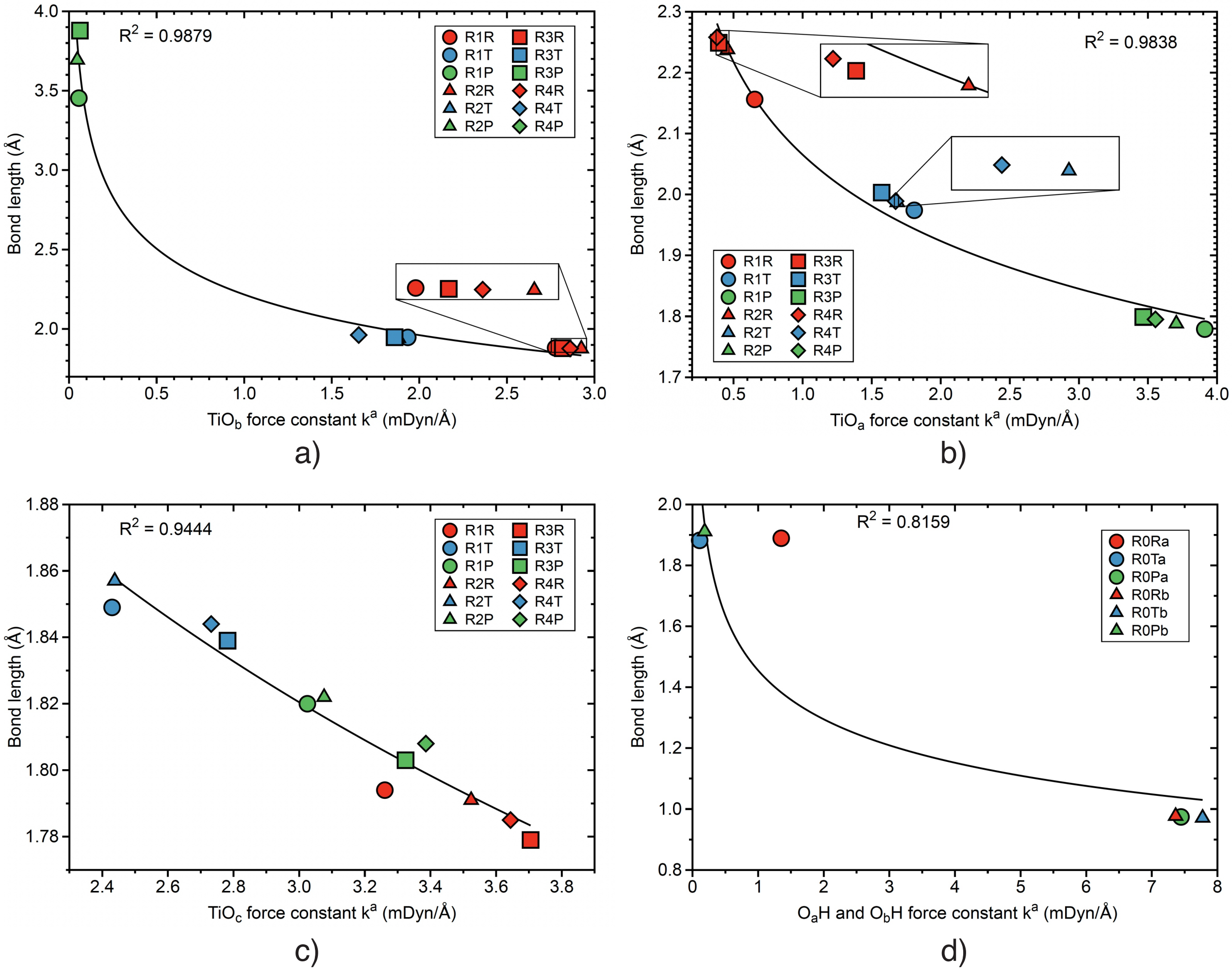

Figure 14. Correlation between bond lengths and the local mode force constants. (**a**–**c**) TiO_b, TiO_a and TiO_c bonds (**d**) O_aH and O_bH bonds. RnR, RnT and RnP indicate the reactant (red color), TS (blue color) and product (green color) for reactions **Rn**, with n=0,$\cdots$4. B3LYP/6-31G(d,p)/SDD(Ti) level of theory.

OH bonds: The non–catalyzed reaction **R0** involves besides OO bond breakage and breakage of the OH peroxide bond (O_bH), followed by hydrogen migration and the formation of a new OH bond (O_aH), as sketched in Figure 2, a process that, according to URVA, results adds considerably to the activation energy. As shown by the data in Table 4, the O_bH bond of the methyl–hydroperoxide reactant has a d(O_bH) distance of 0.977 Å , k^a(O_bH) of 7.363 mDyn/Å, BSO of 0.961 and H_ρ of –0.5863 Hr/Bohr^3, i.e., typical values of a covalent OH bond [116].

Interesting to note is that at the TS the O_bH bond becomes slightly shorter and stronger: d(O_bH) = 0.971 Å, k^a(O_bH) = 7.774 mDyn/Åand BSO = 0.980 and more covalent with H_ρ = –0.6059 Hr/Bohr^3 before reaching the final values of d(O_bH) = 1.911 Å, k^a(O_bH) = 0.185 mDyn/Å, BSO = 0.255 and H_ρ = –0.0015 Hr/Bohr^3 being typical of a very weak hydrogen interaction [116]. The O_aH distance in the reactant is 1.889 Å and a k^a(O_aH) value of 1.352 mDyn/Å and BSO value of 0.522 denoting already some interaction, although no bond O_aH bond critical point was found.

In the TS, the O_aH interaction becomes even weaker (k^a(O_aH) = 1.109 mDyn/Å and BSO = 0.210) although O_aH distance has slightly decreased to 1.882 Å. Again, no bond critical point was found. In the product, the covalent O_aH bond is fully developed with a O_aH distance of 0.974 Å, k^a(O_aH) = 7.445 mDyn/Å, BSO = 0.965 and H_ρ(O_aH) = –0.5828 Hr/Bohr^3 holding the product van der Waals complex together via weak, electrostatic O_bH interactions (see also Figures 10d, 12d and 14d).

4. Conclusions

We investigated, in this work, the catalytic effect of a Sharpless dimeric titanium (IV)–tartrate–diester catalyst on the epoxidation of allylalcohol with methyl–hydroperoxide considering four different orientations of the reacting species coordinated to one of the Ti atoms (reactions **R1**–**R4**) as well as a model for the non–catalyzed reaction (reaction **R0**). As major analysis tools, we applied URVA and LMA, both based on vibrational spectroscopy, complemented by QTAIM analyzing electron density features at the DFT level of theory. The energetics of each reaction were recalculated at the DLPNO-CCSD(T) level of theory. The most important findings of our study can be summarized as follows.

- The dimeric Ti catalyst mimics a surface typical of the heterogenous catalysis, thereby, facilitating a stereospecific reaction. Both ends of the peroxide OO bond coordinate with the Ti atom. The metal atom polarizes the oxygen atoms, facilitating OO bond breakage. The dimeric Ti catalyst smoothly channels the peroxide oxidant into a central position for the attack of the CC double bond of the allyl alcohol, which is coordinated in such a way as to allow allyl group rotations for optimal orientation.
- As revealed by URVA, the overall curvature patterns were similar for all reactions investigated in this work. The chemical event mainly responsible for the activation energy was the cleavage of the peroxide OO bond and, in second order, the start of CO epoxide bond formation accompanied by changes of the TiO bonds for the catalyzed reactions **R1**–**R4** and changes of the OH bonds for the non-catalyzed reaction **R0**. The actual rehybridization of target carbon atoms from sp^2 to sp^3 occurs after the transition state, which does not require energy.

  The same holds for the finalization of the new CO epoxide bonds; therefore, catalyst optimization should predominantly focus on improving OO breakage. Different orientations of the reactants on the quasi-surface spanned by the titanium catalyst affect the reaction mechanism only marginally, mostly with regard to the degree of the synchronicity of CO bond finalization, which may be different for both hydroperoxides and/or allylic alcohols with bulky substituents.
- The strong catalytic effect of the Sharpless catalyst in reducing the unfavorable activation energy of 38 kcal/mol in the non–catalyzed reaction to 22–24 kcal/mol in the catalyzed reaction is documented by the analysis of the energy contribution of each reaction phase (before the TS) to the activation energy barrier. The energy contribution of the dominant OO curvature peak to the activation energy barrier is reduced from 20.7 kcal/mol, in the non–catalyzed reaction to 13–15 kcal/mol, in the catalyzed reaction. In addition, the energy contribution of the OH curvature peak of 11.4 kcal/mol

in the non–catalyzed reaction is replaced by small energy contributions of the TiO curvature peaks in the catalyzed reaction.

- The complementary LMA analysis at all stationary points quantifies that the OO bond of the oxidizing peroxide is weakened upon coordination at the metal atom facilitating OO bond breakage. A more synchronous formation of the new CO epoxide bonds correlates with smaller bond strength differences between these CO bonds, illustrating that the local mode force constant serves as a sensitive tool monitoring the different electronic environments caused by the different orientation of the peroxide and allylalcohol on the catalyst. LMA also elucidates the different roles of the three TiO bonds; TiO_a, coordinating the $\mathrm{OCH_3}$ part of the methyl–hydroperoxide; TiO_c, coordinating the $\mathrm{OCH_2}$ part of the allylalcohol; and the mechanistically most important TiO_b, coordinating the O_b atom of the peroxide being transferred to the CC double bond of allylalcohol for the epoxide bond formation.

  The TiO_c bond is identified as a *spectator* bond, fixing the allylalcohol during the epoxidation reaction accounting and versus weaker TiO_b product bonds versus weaker reactant TiO_a and stronger TiO_a product bonds, with almost equally strong TiO_a and TiO_b bonds at the TS. This shows that the Sharpless catalyst does much more than weakening the OO bond to be broken—it carefully orchestras the entire epoxidation event.

We hope that this article will inspire the computational community to use in the future URVA complemented with LMA as a mechanistic tool for optimization and fine-tuning of current Sharpless catalysts and for the design new of catalysts for epoxidation reactions.

Supplementary Materials: The following supporting information can be downloaded at: https://www.mdpi.com/article/10.3390/catal12070789/s1, containing reaction movies **R0**–**R4** and the Cartesian coordinates of the stationary point, i.e, the reactant van der Waals complex, TS and product of the van der Waals complex for all five reactions **R0**–**R4**.

Author Contributions: Conceptualization; E.K. and M.F.; methodology, M.F. and E.K.; validation,E.K. and M.F. ; formal analysis, M.F. and E.K.; investigation, M.F. and E.K.; resources, E.K.; data curation, M.F.; writing—original draft preparation, M.F.; writing—review and editing, E.K.; funding acquisition, E.K. All authors have read and agreed to the published version of the manuscript.

Funding: This research was funded by the National Science Foundation NSF, grant CHE 2102461.

Data Availability Statement: All data supporting the results of this work are presented in tables and figure of the manuscript and in the Supplementary Materials.

Acknowledgments: We thank the Center for Research Computation at SMU for providing generous high-performance computational resources. We also thank Pratanphorn Nakliang for preliminary work.

Conflicts of Interest: The authors declare no conflict of interest.

References

1. Tomboc, G.M.; Park, Y.; Lee, K.; Jin, K. Directing transition metal-based oxygen-functionalization catalysis. *Chem. Sci.* **2021**, *12*, 8967–8995.
2. Meninno, S.; Lattanzi, A. Epoxides: Small Rings to Play with under Asymmetric Organocatalysis. *ACS Org. Inorg. Au* **2022**. https://doi.org/10.1021/acsorginorgau.2c00009.
3. Philip, R.M.; Radhika, S.; Afsina Abdulla, C.M.; Anilkumar, G. Directing transition metal-based oxygen-functionalization catalysis. *Adv. Synth. Catal.* **2021**, *363*, 1272–1289.
4. Yan, Z.; Tian, J.; Wang, K.; Nigam, K.D.; Luo, G. Microreaction processes for synthesis and utilization of epoxides: A review. *Chem. Eng. Sci.* **2021**, *229*, 116071.
5. Verma, S.; Joshi, A.; De, S.R.; Jat, J.L. Methyltrioxorhenium (MTO) catalysis in the epoxidation of alkenes: A synthetic overview. *New J. Chem.* **2021**, *46*, 2005–2027.
6. Ahmat, Y.M.; Madadi, S.; Charbonneau, L.; Kaliaguine, S. Epoxidation of Terpenes. *Catalysts* **2021**, *11*, 847.
7. Meng, Y.; Taddeo, F.; Freites Aguilera, A.; Cai, X.; Russo, V.; Tolvanen, P.; Leveneur, S. The Lord of the Chemical Rings: Catalytic Synthesis of Important Industrial Epoxide Compounds. *Catalysis* **2021**, *11*, 765.
8. Sharma, S.K.; Paniraj, A.S.R.; Tambe, Y.B. Developments in the Catalytic Asymmetric Synthesis of Agrochemicals and Their Synthetic Importance. *J. Agric. Food Chem.* **2021**, *69*, 14761–14780.

9. Kaur, B.; Singh, P. Epoxides: Developability as active pharmaceutical ingredients and biochemical probes. *Bioorg. Chem.* **2022**, *125*, 105862.
10. Yan, W.; Wang, Z.; Luo, C.; Xia, X.; Liu, Z.; Zhao, Y.; Du, F.; Jin, X. Opportunities and Emerging Challenges of the Heterogeneous Metal-Based Catalysts for Vegetable Oil Epoxidation. *ACS Sustain. Chem. Eng.* **2022**, *10*, 7426–7446. https://doi.org/10.1021/acssuschemeng.2c00617.
11. Zhang, Y.Q.; Poppel, C.; Panfilova, A.; Bohle, F.; Grimme, S.; Gansäuer, A. SN 2 Reactions at Tertiary Carbon Centers in Epoxides. *Angew. Chem. Int. Ed.* **2017**, *56*, 9719–9722.
12. Heravi, M.M.; Lashaki, T.B.; Poorahmad, N. Applications of Sharpless Asymmetric Epoxidation in Total Synthesis. *Tetrahedron Asymmetry* **2015**, *26*, 405–495.
13. Kuznetsov, M.L.; Rocha, B.G.M.; Pombeiro, A.J.L.; Shulpin, G.B. Oxidation of Olefins with Hydrogen Peroxide Catalyzed by Bismuth Salts: A Mechanistic Study. *ACS Catal.* **2015**, *5*, 3823–3835.
14. Huber, S.; Cokoja, M.; Kühn, F.E. Historical Landmarks of The Application of Molecular Transition Metal Catalysts for Olefin Epoxidation. *J. Organ. Chem.* **2014**, *751*, 25–32.
15. Cavani, F.; Teles, J.H. Sustainability in Catalytic Oxidation: An Alternative Approach or a Structural Evolution? *ChemSusChem* **2009**, *2*, 508–534.
16. Roberts, S.M.; Whittall, J. *Catalysts for Fine Chemical Synthesis Regio- and Stereocontrolled Oxidation and Reductions*; John Wiley & Sons: Hoboken, NJ, USA, 2007.
17. Hanzlik, R.P.; Shearer, G.O. Transition State Structure for Peracid Epoxidation. Secondary Deuterium Isotope Effects. *J. Am. Chem. Soc.* **1975**, *97*, 5231–5233.
18. Milchert, E.; Goc, W.; Meissner, E.; Myszkowski, J. Dehydrochlorination of Propylene Chlorohydrin with Sodium Hydroxide and with Catholyte. *J. Chem. Technol. Biotechnol.* **1994**, *61*, 251–254.
19. Freccero, M.; Gandolfi, R.; Sarzi-Amadè, M.; Rastelli, A. Facial Selectivity in Epoxidation of 2-Cyclohexen-1-ol with Peroxy Acids. A Computational DFT Study. *J. Org. Chem.* **2000**, *65*, 8948–8959.
20. Trent, D.L. Propylene Oxide. In *Kirk–Othmer Encyclopedia of Chemical Technology*; American Cancer Society: Atlanta, GA, USA, 2001.
21. Bach, R.D.; Dmitrenko, O.; Adam, W.; Schambony, S. Relative Reactivity of Peracids versus Dioxiranes (DMDO and TFDO) in the Epoxidation of Alkenes. A Combined Experimental and Theoretical Analysis. *J. Am. Chem. Soc.* **2003**, *125*, 924–934.
22. Dmitrenko, O.; Bach, R.D. Reassessment of the Level of Theory Required for the Epoxidation of Ethylene with Dioxiranes. *J. Phys. Chem. A* **2004**, *108*, 6886–6892.
23. Coleman, T.; Kirk, A.M.; Chao, R.R.; Podgorski, M.N.; Harbort, J.S.; Churchman, L.R.; Bruning, J.B.; Paul V., B.; Harmer, J.R.; Krenske, E.H.; et al. Understanding the Mechanistic Requirements for Efficient and Stereoselective Alkene Epoxidation by a Cytochrome P450 Enzyme. *ACS Catal.* **2021**, *11*, 1995–2010.
24. Martínez, S.; Veth, L.; Lainer, B.; Dydio, P. Challenges and Opportunities in Multicatalysis. *ACS Catal.* **2021**, *11*, 3891–3915.
25. Babot, E.D.; Martínez, A.T.; Aranda, C.; Kiebist, J.; Scheibner, K.; Ullrich, R.; Hofrichter, M.; Gutiérrez, A. Enzymatic Epoxidation of Long-Chain Terminal Alkenes by Fungal Peroxygenases. *Antioxidants* **2022**, *11*, 522.
26. Toplak, M.; Matthews, A.; Teufel, R. The devil is in the details: The chemical basis and mechanistic versatility of flavoprotein monooxygenases. *Arch. Biochem. Biophys.* **2021**, *698*, 108732.
27. Sawano, T.; Yamamoto, H. Regio- and Enantioselective Substrate-Directed Epoxidation. *Eur. J. Org. Chem.* **2020**, *2020*, 2369–2378.
28. Wang, K.; Niu, S.; Guo, X.; Tang, W.; Xue, D.; Xiao, J.; Sun, H.; Wan, C. Asymmetric Hydrogenation of Racemic Allylic Alcohols via an Isomerization-Dynamic Kinetic Resolution Cascade. *J. Org. Chem.* **2022**, *12*, 3804–3809.
29. Li, J.J. Sharpless Asymmetric Epoxidation. In *Name Reactions: A Collection of Detailed Mechanisms and Synthetic Applications*; Springer International Publishing: Cambridge, UK, 2021; pp. 497–500.
30. Sartori, S.K.; Miranda, I.L.; Diaz, M.A.N.; Diaz-Munoz, G. Sharpless Asymmetric Epoxidation: Applications in the Synthesis of Bioactive Natural Products. *Mini-Rev. Org. Chem.* **2015**, *18*, 606–620.
31. Porta, R.; Benaglia, M.; Puglisi, A. Flow Chemistry: Recent Developments in the Synthesis of Pharmaceutical Products. *Org. Process Res. Dev.* **2016**, *20*, 2–25.
32. Hyun, Y.E.; Kim, H.R.; Choi, Y.; Jeong, L.S. Stereoselective Synthesis of Anti-Hepatitis B Drug, Entecavir, through Regio- and Stereoselective Epoxide Cleavage. *Asian J. Org. Chem.* **2017**, *6*, 1213–1218.
33. Bhadra, S.; Yamamoto, H. Substrate Directed Asymmetric Reactions. *Chem. Rev.* **2018**, *118*, 3391–3446.
34. Moschona, F.; Savvopoulou, I.; Tsitopoulou, M.; Tataraki, D.; Rassias, G. Epoxide Syntheses and Ring–Opening Reactions in Drug Development. *Catalysts* **2020**, *10*, 1117–1182.
35. Petsi, M.; Orfanidou, M.; Zografos, A.L. Organocatalytic epoxidation and allylic oxidation of alkenes by molecular oxygen. *Green Chem.* **2021**, *23*, 9172–9178.
36. Triandafillidi, I.; Kokotou, M.G.; Lotter, D.; Sparr, C.; Kokotos, C.G. Aldehyde-catalyzed epoxidation of unactivated alkenes with aqueous hydrogen peroxide. *Chem. Sci.* **2021**, *12*, 10191–10196.
37. Wang, C.; Yamamoto, H. Asymmetric Epoxidation Using Hydrogen Peroxide as Oxidant. *Chem. Asian J.* **2015**, *10*, 2056–2068.
38. Salmi, T.; Aguilera, A.F.; Lindroos, P.; Kanerva, L. Mathematical modelling of oleic acid epoxidation via a chemo-enzymatic route—From reaction mechanisms to reactor model. *Chem. Eng. Sci.* **2022**, *247*, 117047.

39. Sharpless, K.B.; Verhoeven, T.R. Metal-Catalyzed, Highly Selective Oxygenation of Olefins and Acetylene with *tert*-Butyl Hydroperoxide Pratical Considerations and Mechanisms. *Aldrichim. Acta* **1979**, *12*, 63–74.
40. Katsuki, T.; Sharpless, K.B. The First Practical Method for Asymmetric Epoxidation. *J. Am. Chem. Soc.* **1980**, *102*, 5974–5976.
41. Sharpless, K.B. Searching for New Reactivity (Nobel Lecture). *Ang. Chem. Int. Ed.* **2002**, *41*, 2024.
42. Rossiter, B.E.; Katsuki, T.; Sharpless, K.B. Asymmetric Epoxidation Provides Shortest Routes to Four Chiral Epoxy Alcohols Which are Key Intermediates in Syntheses of Methymycin, Erythromycin, Leukotriene C-1, and Disparlure. *J. Am. Chem. Soc.* **1981**, *103*, 464–465.
43. Lu, L.D.L.; Johnson, R.A.; Finn, M.G.; Sharpless, K.B. Two New Asymmetric Epoxidation Catalysts. Unusual Stoichiometry and Inverse Enantiofacial Selection. *J. Org. Chem.* **1984**, *49*, 728–731.
44. Williams, I.D.; Pedersen, S.F.; Sharpless, K.B.; Lippard, S.J. Crystal Structures of Two Titanium Tartrate Asymmetric Epoxidation Catalysts. *J. Am. Chem. Soc.* **1984**, *106*, 6430–6431.
45. Gao, Y.; Klunder, J.M.; Hanson, R.M.; Masamune, H.; Ko, S.Y.; Sharpless, K.B. Catalytic Asymmetric Epoxidation and Kinetic Resolution: Modified Procedures Including in Situ Derivatization. *J. Am. Chem. Soc.* **1987**, *109*, 5765–5780.
46. Pedersen, S.F.; Dewan, J.C.; Eckman, R.R.; Sharpless, K.B. Unexpected Diversity in the Coordination Chemistry of Tartrate Esters with Titanium(IV). *J. Am. Chem. Soc.* **1987**, *109*, 1279–1282.
47. Carlier, P.R.; Sharpless, K.B. Studies on the Mechanism of the Ssymmetric Epoxidation: A Ligand Variation Approach. *J. Org. Chem.* **1989**, *54*, 4016–4018.
48. Woodard, S.S.; Finn, M.G.; Sharpless, K.B. Mechanism of asymmetric epoxidation. 1. Kinetics. *J. Am. Chem. Soc.* **1991**, *113*, 106–113.
49. Finn, M.G.; Sharpless, K.B. Mechanism of Asymmetric Epoxidation. 2. Catalyst Structure. *J. Am. Chem. Soc.* **1991**, *113*, 113–126.
50. Berrisford, D.J.; Bolm, C.; Sharpless, K.B. Ligand-Accelerated Catalysis. *Angew. Chem. Int. Ed.* **1995**, *34*, 1059–1070.
51. Katsuki, T.; Martin, V. Asymmetric Epoxidation of Allylic Alcohols: The Katsuki–Sharpless Epoxidation Reaction. In *Organic Reactions*; American Cancer Society: Atlanta, GA, USA, 2004; Chapter 1, pp. 1–299.
52. Astruc, D. *Organometallic Chemistry and Catalysis*; Springer: Berlin/Heidelberg, Germany, 2007.
53. Borrell, M.; Costas, M. Greening Oxidation Catalysis: Iron Catalyzed Alkene syn-Dihydroxylation with Aqueous Hydrogen Peroxide in Green Solvents. *ACS Sustain. Chem. Eng.* **2018**, *6*, 8410–8416.
54. Ramón, D.J.; Yus, M. In the Arena of Enantioselective Synthesis, Titanium Complexes Wear the Laurel Wreath. *Chem. Rev.* **2006**, *106*, 2126–2208.
55. Kuznetsov, M.L.; Pessoa, J.C. Epoxidation of Olefins Catalysed by Vanadium–Salan Complexes: A Theoretical Mechanistic Study. *Dalton Trans.* **2009**, *2009*, 5460.
56. Riera, A.; Moreno, M. Synthetic Applications of Chiral Unsaturated Epoxy Alcohols Prepared by Sharpless Asymmetric Epoxidation. *Molecules* **2010**, *15*, 1041–1073.
57. Bartók, M. Unexpected Inversions in Asymmetric Reactions: Reactions with Chiral Metal Complexes, Chiral Organocatalysts, and Heterogeneous Chiral Catalysts. *Chem. Rev.* **2010**, *110*, 1663–1705.
58. Botubol-Ares, J.M.; Hanson, J.R.; Hernández-Galán, R.; Collado, I.G. Mild Epoxidation of Allylic Alcohols Catalyzed by Titanium(III) Complexes: Selectivity and Mechanism. *ACS Omega* **2017**, *2*, 3083–3090.
59. Sawano, T.; Yamamoto, H. Substrate-Directed Catalytic Selective Chemical Reactions. *J. Org. Chem.* **2018**, *83*, 4889–4904.
60. Fernandes, A.S.; Maître, P.; Correra, T.C. Evaluation of the Katsuki–Sharpless Epoxidation Precatalysts by ESI-FTMS, CID, and IRMPD Spectroscopy. *J. Phys. Chem. A* **2019**, *123*, 1022–1029.
61. Severin, F.; Fusi, G.M.; Wartmann, C.; Neudörfl, J.M.; Berkessel, A. Sharpless Asymmetric Epoxidation: Applications in the Synthesis of Bioactive Natural Products. *Angew. Chem. Int. Ed.* **2022**, e202201790.
62. Feng, X.; Du, H. Shi Epoxidation: A Great Shortcut to Complex Compounds. *Chin. J. Chem.* **2021**, *39*, 2016–2026.
63. List, B.; MacMillan, D. Discovery of Asymmetric Organocatalysis. Nobel Foundation. 2021. Available online: www.nobelprize.org (accessed on 17 June 2022).
64. Bach, R.D.; Schlegel, H.B. Mechanism of Orbital Interactions in the Sharpless Epoxidation with Ti(IV) Peroxides: A DFT Study. *J. Phys. Chem. A* **2021**, *125*, 10541–10556.
65. Jørgensen, K.A.; Wheeler, R.A.; Hoffmann, R. Electronic and Steric Factors Determining the Asymmetric Epoxidation of Allylic Alcohols by Titanium-tartrate Complexes (the Sharpless Epoxidation). *J. Am. Chem. Soc.* **1987**, *109*, 3240–3246.
66. Wu, Y.D.; Lai, D.K.W. A Density Functional Study on the Stereocontrol of the Sharpless Epoxidation. *J. Am. Chem. Soc* **1995**, *117*, 11327–11336.
67. Wu, Y.D.; Lai, D.K.W. Transition Structure for the Epoxidation Mediated by Titanium(IV) Peroxide. A Density Functional Study. *J. Org. Chem.* **1995**, *60*, 673–680.
68. Yudanov, I.V.; Gisdakis, P.; Valentin, C.D.; Rösch, N. Activity of Peroxo and Hydroperoxo Complexes of TiIV in Olefin Epoxidation: A Density Functional Model Study of Energetics and Mechanism. *Eur. J. Inorg. Chem.* **1999**, *1999*, 2135–2145.
69. Cui, M.; Adam, W.; Shen, J.H.; Luo, X.M.; Tan, X.J.; Chen, K.X.; Ji, R.Y.; Jiang, H.L. A Density-Functional Study of the Mechanism for the Diastereoselective Epoxidation of Chiral Allylic Alcohols by the Titanium Peroxy Complexes. *J. Org. Chem.* **2002**, *67*, 1427–1435.
70. Jänner, S.; Isak, D.; Li, Y.; Houk, K.N.; Miller, A.K. Bioinspired Asymmetric Total Synthesis of Emeriones A-C. *ChemRxiv* **2022**, *125*, e202205878.

71. Corey, E.J. On the origin of enantioselectivity in the Katsuki-Sharpless epoxidation procedure. *J. Org. Chem.* **1990**, *55*, 1693–1694.
72. Kraka, E.; Zou, W.; Tao, Y.; Freindorf, M. Exploring the Mechanism of Catalysis with the Unified Reaction Valley Approach (URVA)—A Review. *Catalysts* **2020**, *10*, 691.
73. Kraka, E.; Zou, W.; Tao, Y. Decoding Chemical Information from Vibrational Spectroscopy Data: Local Vibrational Mode Theory. *WIREs Comput. Mol. Sci.* **2020**, *10*, 1480.
74. Bader, R.F.W. *Atoms in Molecules: A Quantum Theory (International Series of Monographs on Chemistry)*; Clarendon Press: Oxford, UK, 1994.
75. Bader, R.F.W. A quantum theory of molecular structure and its applications. *Chem. Rev.* **1991**, *91*, 893–928.
76. Bader, R.F.W. The Quantum Mechanical Basis of Conceptual Chemistry. *Monatshefte Chem.* **2005**, *136*, 819–854.
77. Popelier, P.L. *Atoms in Molecules: An Introduction*; Prentice Hall: Hoboken, NJ, USA, 2000.
78. Reed, A.E.; Curtiss, L.A.; Weinhold, F. Intermolecular Interactions from a Natural Bond Orbital, Donor-Acceptor Viewpoint. *Chem. Rev.* **1988**, *88*, 899–926.
79. Weinhold, F.; Landis, C.R. *Valency and Bonding: A Natural Bond Orbital Donor-Acceptor Perspective*; Cambridge University Press: Cambridge, UK, 2003.
80. Weinhold, F. The Path to Natural Bond Orbitals. *Isr. J. Chem.* **2022**, *62*, e202100026.
81. Zou, W.; Sexton, T.; Kraka, E.; Freindorf, M.; Cremer, D. A New Method for Describing the Mechanism of a Chemical Reaction Based on the Unified Reaction Valley Approach. *J. Chem. Theory Comput.* **2016**, *12*, 650–663.
82. Kraka, E. Reaction Path Hamiltonian and the Unified Reaction Valley Approach. *WIREs Comput. Mol. Sci.* **2011**, *1*, 531–556.
83. Joo, H.; Kraka, E.; Quapp, W.; Cremer, D. The Mechanism of a Barrierless Reaction: Hidden Transition State and Hidden Intermediates in the Reaction of Methylene with Ethene. *Mol. Phys.* **2007**, *105*, 2697–2717.
84. Miller, W.H.; Handy, N.C.; Adams, J.E. Reaction Path Hamiltonian for Polyatomic Molecules. *J. Chem. Phys.* **1980**, *72*, 99–112.
85. Kraka, E.; Cremer, D. Computational Analysis of the Mechanism of Chemical Reactions in Terms of Reaction Phases: Hidden Intermediates and Hidden Transition States. *Acc. Chem. Res.* **2010**, *43*, 591–601.
86. Cremer, D.; Kraka, E. From Molecular Vibrations to Bonding, Chemical Reactions, and Reaction Mechanism. *Curr. Org. Chem.* **2010**, *14*, 1524–1560.
87. Makoś, M.Z.; Freindorf, M.; Tao, Y.; Kraka, E. Theoretical Insights into [NHC]Au(I) Catalyzed Hydroalkoxylation of Allenes: A Unified Reaction Valley Approach Study. *J. Org. Chem.* **2021**, *86*, 5714–5726.
88. Nanayakkara, S.; Freindorf, M.; Tao, Y.; Kraka, E. Modeling Hydrogen release from water with Borane and Alane catalysts: A Unified Reaction Valley Approach. *J. Phys. Chem. A* **2020**, *124*, 8978–8993.
89. Tao, Y.; Zou, W.; Nanayakkara, S.; Kraka, E. PyVibMS: A PyMOL plugin for visualizing vibrations in molecules and solids. *J. Mol. Model.* **2020**, *26*, 290-1–290-12.
90. Nanayakkara, S.; Kraka, E. A New Way of Studying Chemical Reactions: A Hand-in-hand URVA and QTAIM Approach. *Phys. Chem. Chem. Phys.* **2019**, *21*, 15007–15018.
91. Freindorf, M.; Tao, Y.; Sethio, D.; Cremer, D.; Kraka, E. New Mechanistic Insights into the Claisen Rearrangement of Chorismate—A Unified Reaction Valley Approach Study. *Mol. Phys.* **2018**, *117*, 1172–1192.
92. Freindorf, M.; Cremer, D.; Kraka, E. Gold(I)-Assisted Catalysis—A Comprehensive View on the [3,3]-Sigmatropic Rearrangement of Allyl Acetate. *Mol. Phys.* **2017**, *116*, 611–630.
93. Reis, M.C.; López, C.S.; Kraka, E.; Cremer, D.; Faza, O.N. Rational Design in Catalysis: A Mechanistic Study of β-Hydride Eliminations in Gold(I) and Gold(III) Complexes Based on Features of the Reaction Valley. *Inorg. Chem.* **2016**, *55*, 8636–8645.
94. Sexton, T.; Kraka, E.; Cremer, D. Extraordinary Mechanism of the Diels-Alder Reaction: Investigation of Stereochemistry, Charge Transfer, Charge Polarization, and Biradicaloid Formation. *J. Phys. Chem. A* **2016**, *120*, 1097–1111.
95. Konkoli, Z.; Cremer, D. A New Way of Analyzing Vibrational Spectra. I. Derivation of Adiabatic Internal Modes. *Int. J. Quantum Chem.* **1998**, *67*, 1–9.
96. Konkoli, Z.; Larsson, J.A.; Cremer, D. A New Way of Analyzing Vibrational Spectra. II. Comparison of Internal Mode Frequencies. *Int. J. Quantum Chem.* **1998**, *67*, 11–27.
97. Konkoli, Z.; Cremer, D. A New Way of Analyzing Vibrational Spectra. III. Characterization of Normal Vibrational Modes in terms of Internal Vibrational Modes. *Int. J. Quantum Chem.* **1998**, *67*, 29–40.
98. Konkoli, Z.; Larsson, J.A.; Cremer, D. A New Way of Analyzing Vibrational Spectra. IV. Application and Testing of Adiabatic Modes within the Concept of the Characterization of Normal Modes. *Int. J. Quantum Chem.* **1998**, *67*, 41–55.
99. Cremer, D.; Larsson, J.A.; Kraka, E. New Developments in the Analysis of Vibrational Spectra on the Use of Adiabatic Internal Vibrational Modes. In *Theoretical and Computational Chemistry*; Parkanyi, C., Ed.; Elsevier: Amsterdam, The Netherlands, 1998; pp. 259–327.
100. Wilson, E.; Decius, J.; Cross, P. *Molecular Vibrations. The Theory of Infrared and Raman Vibrational Spectra*; McGraw-Hill: New York, NY, USA, 1955.
101. Woodward, L.A. *Introduction to the Theory of Molecular Vibrations and Vibrational Spectroscopy*; Oxford University Press: Oxford, UK, 1972.
102. Zou, W.; Cremer, D. C_2 in a Box: Determining its Intrinsic Bond Strength for the $X^1\ \Sigma^+{}_g$ Ground State. *Chem. Eur. J.* **2016**, *22*, 4087–4097.

103. Larsson, J.A.; Cremer, D. Theoretical Verification and Extension of the Mckean Relationship between Bond Lengths and Stretching Frequencies. *J. Mol. Struct.* **1999**, *485–486*, 385–407.
104. Kalescky, R.; Kraka, E.; Cremer, D. Identification of the Strongest Bonds in Chemistry. *J. Phys. Chem. A* **2013**, *117*, 8981–8995.
105. Setiawan, D.; Sethio, D.; Cremer, D.; Kraka, E. From Strong to Weak NF Bonds: On the Design of a New Class of Fluorinating Agents. *Phys. Chem. Chem. Phys.* **2018**, *20*, 23913–23927.
106. Humason, A.; Zou, W.; Cremer, D. 11,11-Dimethyl-1,6-methano[10]annulene-An Annulene with an Ultralong CC Bond or a Fluxional Molecule? *J. Phys. Chem. A* **2014**, *119*, 1666–1682.
107. Kalescky, R.; Kraka, E.; Cremer, D. Are Carbon-Halogen Double and Triple Bonds Possible? *Int. J. Quantum Chem.* **2014**, *114*, 1060–1072.
108. Kalescky, R.; Zou, W.; Kraka, E.; Cremer, D. Quantitative Assessment of the Multiplicity of Carbon-Halogen Bonds: Carbenium and Halonium Ions with F, Cl, Br, and I. *J. Phys. Chem. A* **2014**, *118*, 1948–1963.
109. Cremer, D.; Wu, A.; Larsson, J.A.; Kraka, E. Some Thoughts about Bond Energies, Bond Lengths, and Force Constants. *J. Mol. Model.* **2000**, *6*, 396–412.
110. Kraka, E.; Cremer, D. Weaker Bonds with Shorter Bond Lengths. *Rev. Proc. Quim.* **2012**, *6*, 39–42.
111. Setiawan, D.; Kraka, E.; Cremer, D. Hidden Bond Anomalies: The Peculiar Case of the Fluorinated Amine Chalcogenides. *J. Phys. Chem. A* **2015**, *119*, 9541–9556.
112. Kraka, E.; Setiawan, D.; Cremer, D. Re-Evaluation of the Bond Length-Bond Strength Rule: The Stronger Bond Is not Always the Shorter Bond. *J. Comp. Chem.* **2015**, *37*, 130–142.
113. Delgado, A.A.A.; Humason, A.; Kalescky, R.; Freindorf, M.; Kraka, E. Exceptionally Long Covalent CC Bonds—A Local Vibrational Mode Study. *Molecules* **2021**, *26*, 950.
114. Kalescky, R.; Zou, W.; Kraka, E.; Cremer, D. Local Vibrational Modes of the Water Dimer—Comparison of Theory and Experiment. *Chem. Phys. Lett.* **2012**, *554*, 243–247.
115. Kalescky, R.; Kraka, E.; Cremer, D. Local Vibrational Modes of the Formic Acid Dimer—The Strength of the Double H-Bond. *Mol. Phys.* **2013**, *111*, 1497–1510.
116. Freindorf, M.; Kraka, E.; Cremer, D. A Comprehensive Analysis of Hydrogen Bond Interactions Based on Local Vibrational Modes. *Int. J. Quantum Chem.* **2012**, *112*, 3174–3187.
117. Kalescky, R.; Zou, W.; Kraka, E.; Cremer, D. Vibrational Properties of the Isotopomers of the Water Dimer Derived from Experiment and Computations. *Aust. J. Chem.* **2014**, *67*, 426.
118. Tao, Y.; Zou, W.; Jia, J.; Li, W.; Cremer, D. Different Ways of Hydrogen Bonding in Water—Why Does Warm Water Freeze Faster than Cold Water? *J. Chem. Theory Comput.* **2017**, *13*, 55–76.
119. Tao, Y.; Zou, W.; Kraka, E. Strengthening of Hydrogen Bonding With the Push-Pull Effect. *Chem. Phys. Lett.* **2017**, *685*, 251–258.
120. Makoś, M.Z.; Freindorf, M.; Sethio, D.; Kraka, E. New Insights into Fe–H_2 and Fe–H^- Bonding of a [NiFe] Hydrogenase Mimic—A Local Vibrational Mode Study. *Theor. Chem. Acc.* **2019**, *138*, 76.
121. Lyu, S.; Beiranvand, N.; Freindorf, M.; Kraka, E. Interplay of Ring Puckering and Hydrogen Bonding in Deoxyribonucleosides. *J. Phys. Chem. A* **2019**, *123*, 7087–7103.
122. Yannacone, S.; Sethio, D.; Kraka, E. Quantitative Assessment of Intramolecular Hydrogen Bonds in Neutral Histidine. *Theor. Chem. Acc.* **2020**, *139*, 125.
123. Oliveira, V.; Kraka, E.; Cremer, D. The Intrinsic Strength of the Halogen Bond: Electrostatic and Covalent Contributions Described by Coupled Cluster Theory. *Phys. Chem. Chem. Phys.* **2016**, *18*, 33031–33046.
124. Oliveira, V.; Kraka, E.; Cremer, D. Quantitative Assessment of Halogen Bonding Utilizing Vibrational Spectroscopy. *Inorg. Chem.* **2016**, *56*, 488–502.
125. Oliveira, V.; Cremer, D. Transition from Metal-Ligand Bonding to Halogen Bonding Involving a Metal as Halogen Acceptor: A Study of Cu, Ag, Au, Pt, and Hg Complexes. *Chem. Phys. Lett.* **2017**, *681*, 56–63.
126. Yannacone, S.; Oliveira, V.; Verma, N.; Kraka, E. A Continuum from Halogen Bonds to Covalent Bonds: Where Do λ^3 Iodanes Fit? *Inorganics* **2019**, *7*, 47.
127. Oliveira, V.P.; Kraka, E.; Machado, F.B.C. Pushing 3c-4e Bonds to the Limit: A Coupled Cluster Study of Stepwise Fluorination of First-Row Atoms. *Inorg. Chem.* **2019**, *58*, 14777–14789.
128. Oliveira, V.P.; Marcial, B.L.; Machado, F.B.C.; Kraka, E. Metal-Halogen Bonding Seen through the Eyes of Vibrational Spectroscopy. *Materials* **2020**, *13*, 55.
129. Oliveira, V.; Kraka, E. Systematic Coupled Cluster Study of Noncovalent Interactions Involving Halogens, Chalcogens, and Pnicogens. *J. Phys. Chem. A* **2017**, *121*, 9544–9556.
130. Setiawan, D.; Kraka, E.; Cremer, D. Description of Pnicogen Bonding with the help of Vibrational Spectroscopy-The Missing Link Between Theory and Experiment. *Chem. Phys. Lett.* **2014**, *614*, 136–142.
131. Setiawan, D.; Kraka, E.; Cremer, D. Strength of the Pnicogen Bond in Complexes Involving Group VA Elements N, P, and As. *J. Phys. Chem. A* **2014**, *119*, 1642–1656.
132. Setiawan, D.; Cremer, D. Super-Pnicogen Bonding in the Radical Anion of the Fluorophosphine Dimer. *Chem. Phys. Lett.* **2016**, *662*, 182–187.
133. Oliveira, V.; Cremer, D.; Kraka, E. The Many Facets of Chalcogen Bonding: Described by Vibrational Spectroscopy. *J. Phys. Chem. A* **2017**, *121*, 6845–6862.

134. Sethio, D.; Oliveira, V.; Kraka, E. Quantitative Assessment of Tetrel Bonding Utilizing Vibrational Spectroscopy. *Molecules* **2018**, *23*, 2763.
135. Zhang, X.; Dai, H.; Yan, H.; Zou, W.; Cremer, D. B-H π Interaction: A New Type of Nonclassical Hydrogen Bonding. *J. Am. Chem. Soc.* **2016**, *138*, 4334–4337.
136. Zou, W.; Zhang, X.; Dai, H.; Yan, H.; Cremer, D.; Kraka, E. Description of an Unusual Hydrogen Bond Between Carborane and a Phenyl Group. *J. Organometal. Chem.* **2018**, *856*, 114–127.
137. Setiawan, D.; Kraka, E.; Cremer, D. Quantitative Assessment of Aromaticity and Antiaromaticity Utilizing Vibrational Spectroscopy. *J. Org. Chem.* **2016**, *81*, 9669–9686.
138. Li, Y.; Oliveira, V.; Tang, C.; Cremer, D.; Liu, C.; Ma, J. The Peculiar Role of the Au_3 Unit in Au_m Clusters: σ-Aromaticity of the Au_5Zn^+ Ion. *Inorg. Chem.* **2017**, *56*, 5793–5803.
139. Kalescky, R.; Kraka, E.; Cremer, D. Description of Aromaticity with the Help of Vibrational Spectroscopy: Anthracene and Phenanthrene. *J. Phys. Chem. A* **2013**, *118*, 223–237.
140. Kalescky, R.; Kraka, E.; Cremer, D. New Approach to Tolman's Electronic Parameter Based on Local Vibrational Modes. *Inorg. Chem.* **2013**, *53*, 478–495.
141. Setiawan, D.; Kalescky, R.; Kraka, E.; Cremer, D. Direct Measure of Metal-Ligand Bonding Replacing the Tolman Electronic Parameter. *Inorg. Chem.* **2016**, *55*, 2332–2344.
142. Cremer, D.; Kraka, E. Generalization of the Tolman Electronic Parameter: The Metal-Ligand Electronic Parameter and the Intrinsic Strength of the Metal-Ligand Bond. *Dalton Trans.* **2017**, *46*, 8323–8338.
143. Li, Y.; Liu, C.; Oliveira, V.; Cremer, D.; Chen, Z.; Ma, J. Odd-even Effect of the Number of Free Valence Electrons on the Electronic Structure Properties of Gold-thiolate Clusters. *Mol. Phys.* **2018**, *117*, 1442–1450.
144. Kraka, E.; Freindorf, M. Characterizing the Metal Ligand Bond Strength via Vibrational Spectroscopy: The Metal Ligand Electronic Parameter (MLEP). In *Topics in Organometallic Chemistry—New Directions in the Modeling of Organometallic Reactions*; Lledós, A., Ujaque, G., Eds.; Springer: Berlin/Heidelberg, Germany, 2020; Volume 67, pp. 1–43.
145. Verma, N.; Tao, Y.; Zou, W.; Chen, X.; Chen, X.; Freindorf, M.; Kraka, E. A Critical Evaluation of Vibrational Stark Effect (VSE) Probes with the Local Vibrational Mode Theory. *Sensors* **2020**, *20*, 2358.
146. Zou, W.; Tao, Y.; Freindorf, M.; Cremer, D.; Kraka, E. Local Vibrational Force Constants—From the Assessment of Empirical Force Constants to the Description of Bonding in Large Systems. *Chem. Phys. Lett.* **2020**, *478*, 137337.
147. Freindorf, M.; Kraka, E. Critical Assessment of the FeC and CO Bond strength in Carboxymyoglobin—A QM/MM Local Vibrational Mode Study. *J. Mol. Model.* **2020**, *26*, 281.
148. Beiranvand, N.; Freindorf, M.; Kraka, E. Hydrogen Bonding in Natural and Unnatural Base Pairs—Explored with Vibrational Spectroscopy. *Molecules* **2021**, *26*, 2268.
149. Tao, Y.; Zou, W.; Sethio, D.; Verma, N.; Qiu, Y.; Tian, C.; Cremer, D.; Kraka, E. In Situ Measure of Intrinsic Bond Strength in Crystalline Structures: Local Vibrational Mode Theory for Periodic Systems. *J. Chem. Theory Comput.* **2019**, *15*, 1761–1776.
150. Tao, Y.; Qiu, Y.; Zou, W.; Nanayakkara, S.; Yannacone, S.; Kraka, E. In Situ Assessment of Intrinsic Strength of X-I$\cdots$OA Type Halogen Bonds in Molecular Crystals with Periodic Local Vibrational Mode Theory. *Molecules* **2020**, *25*, 1589.
151. Kraka, E.; Larsson, J.A.; Cremer, D. Generalization of the Badger Rule Based on the Use of Adiabatic Vibrational Modes. In *Computational Spectroscopy*; Grunenberg, J., Ed.; Wiley: New York, NY, USA, 2010; pp. 105–149.
152. Mayer, I. Charge, bond brder an valence in the ab initio theory. *Chem. Phys. Lett.* **1983**, *97*, 270–274.
153. Mayer, I. Bond orders and valences from ab initio wave functions. *Int. J. Quantum Chem.* **1986**, *29*, 477–483.
154. Mayer, I. Bond order and valence indices: A personal account. *J. Comput. Chem.* **2007**, *28*, 204–221. https://doi.org/10.1002/jcc.20494.
155. Cremer, D.; Kraka, E. Chemical Bonds without Bonding Electron Density? Does the Difference Electron-Density Analysis Suffice for a Description of the Chemical Bond? *Angew. Chem. Int. Ed.* **1984**, *23*, 627–628.
156. Cremer, D.; Kraka, E. A Description of the Chemical Bond in Terms of Local Properties of Electron Density and Energy. *Croatica Chem. Acta* **1984**, *57*, 1259–1281.
157. Kraka, E.; Cremer, D. Chemical Implication of Local Features of the Electron Density Distribution. In *Theoretical Models of Chemical Bonding. The Concept of the Chemical Bond*; Maksic, Z.B., Ed.; Springer: Berlin/Heidelberg, Germany, 1990; Volume 2, pp. 453–542.
158. Fukui, K. The Path of Chemical Reactions—The IRC Approach. *Acc. Chem. Res.* **1981**, *14*, 363–368.
159. Hratchian, H.P.; Kraka, E. Improved Predictor-Corrector Integrators For Evaluating Reaction Path Curvature. *J. Chem. Theory Comput.* **2013**, *9*, 1481–1488.
160. Becke, A.D. Density-Functional Thermochemistry. III. The Role of Exact Exchange. *J. Chem. Phys.* **1993**, *98*, 5648–5652.
161. Lee, C.; Yang, W.; Parr, R. Development of the Colle-Salvetti correlation-energy formula into a functional of the electron density. *Phys. Rev. B* **1988**, *37*, 785–789.
162. Vosko, S.; Wilk, L.; Nusair, M. Accurate spin-dependent electron liquid correlation energies for local spin density calculations: A critical analysis. *Can. J. Phys.* **1980**, *58*, 1200–1211.
163. Stephens, P.; Devlin, F.; Chabalowski, C.; Frisch, M. Ab Initio Calculation of Vibrational Absorption and Circular Dichroism Spectra Using Density Functional Force Fields. *J. Phys. Chem.* **1994**, *98*, 11623–11627.
164. McLean, A.D.; Chandler, G.S. Contracted Gaussian basis sets for molecular calculations. I. Second row atoms, Z = 11–18. *J. Chem. Phys.* **1980**, *72*, 5639–5648.

165. Krishnan, R.; Binkley, J.S.; Seeger, R.; Pople, J.A. Self–consistent molecular orbital methods. XX. A basis set for correlated wave functions. *J. Chem. Phys.* **1980**, *72*, 650–654.
166. Andrae, D.; Häußermann, U.; Dolg, M.; Stoll, H.; Preuß, H. Energy–adjusted ab initio pseudopotentials for the second and third row transition elements. *Theoret. Chim. Acta* **1990**, *77*, 123–141.
167. Riplinger, C.; Neese, F. An efficient and near linear scaling pair natural orbital based local coupled cluster method. *J. Chem. Phys.* **2013**, *138*, 034106.
168. Weigend, F.; Ahlrichs, R. Balanced basis sets of split valence, triple zeta valence and quadruple zeta valence quality for H to Rn: Design and assessment of accuracy. *Phys. Chem. Chem. Phys.* **2005**, *7*, 3297–3305.
169. Frisch, M.J.; Trucks, G.W.; Schlegel, H.B.; Scuseria, G.E.; Robb, M.A.; Cheeseman, J.R.; Scalmani, G.; Barone, V.; Mennucci, B.; Petersson, G.A.; et al. *Gaussian 09, Revision D.01*; Gaussian Inc.: Wallingford, CT, USA, 2009.
170. Neese, F. The ORCA program system. *WIREs Comput. Mol. Sci.* **2012**, *2*, 73–78.
171. Tao, Y.; Zou, W.; Freindorf, M.; Cremer, D.; Kraka, E. *pURVA*; Computational and Theoretical Chemistry Group (CATCO), Southern Methodist University: Dallas, TX, USA, 2021.
172. Zou, W.; Tao, Y.; Freindorf, M.; Makoś, M.Z.; Verma, N.; Cremer, D.; Kraka, E. *Local Vibrational Mode Analysis (LModeA)*; Computational and Theoretical Chemistry Group (CATCO), Southern Methodist University: Dallas, TX, USA, 2021.
173. Keith, T.A. *AIMALL*; TK Gristmill Software: Overland Park, KS, USA, 2017.
174. Wu, H.; Wang, L.S. Electronic structure of titanium oxide clusters: TiO_y (y = 1-3) and $(TiO_2)_n$ (n-1-4). *J. Chem. Phys.* **1997**, *107*, 8221–8228.
175. Miliordos, E.; Harrison, J.F.; Hunt, K.L.C. Ab initio investigation of titanium hydroxide isomers and their cations, $TiOH^{0,+}$ and $HTiO^{0,+}$. *J. Chem. Phys.* **2011**, *135*, 144111.
176. Cremer, D.; Kraka, E. Theoretical Determination of Molecular Structure and Conformation. 15. Three-Membered Rings: Bent Bonds, Ring Strain, and Surface Delocalization. *J. Am. Chem. Soc.* **1985**, *107*, 3800–3810.
177. Cremer, D.; Kraka, E. Theoretical Determination of Molecular Structure and Conformation. 16. Substituted Cyclopropanes—An Electron Density Model of Substituent-Ring Interactions. *J. Am. Chem. Soc.* **1985**, *107*, 3811–3819.
178. Cremer, D.; Gauss, J. Theoretical Determination of Molecular Structure and Conformation. 20. Reevaluation of the Strain Energies of Cyclopropane and Cyclobutane Carbon-Carbon and Carbon-Hydrogen Bond Energies, 1,3 Interactions, and σ-Aromaticity. *J. Am. Chem. Soc.* **1986**, *108*, 7467–7477.
179. Cremer, D. Pros and Cons of σ-Aromaticity. *Tetrahedron* **1988**, *44*, 7427–7454.
180. Kraka, E.; Cremer, D. Characterization of CF Bonds with Multiple-Bond Character: Bond Lengths, Stretching Force Constants, and Bond Dissociation Energies. *ChemPhysChem* **2009**, *10*, 686–698.
181. Kaupp, M.; Danovich, D.; Shaik, S. Chemistry is about energy and its changes: A critique of bond-length/bond-strength correlations. *Coord. Chem. Rev.* **2017**, *344*, 355–362.